ABSTRACT OF PhD. THESIS

Applications of DWI and DTI scanning techniques for rapid assessment of specific parameter changes in brain disease

PhD. candidate,

Eng. Lenuța Toporaș (PANĂ)

SCIENTIFIC COORDINATOR,

Prof. PhD. Eng. Phys. Luminița MORARU

IOSUD – „DUNĂREA DE JOS” UNIVERSITY OF GALATI
Doctoral School of Mechanical and Industrial Engineering

UNIVERSITAS

GALATIENSIS

ABSTRACT OF PhD. THESIS

Applications of DWI and DTI scanning techniques for rapid assessment of specific parameter changes in brain disease

PhD. candidate,
Eng. Lenuța Toporaș (PANĂ)

President,	**Prof. PhD. Eng. Elena Scutelnicu** Dean of Faculty of Engineering, "Dunarea de Jos" University of Galati
Scientific Coordinator,	**Prof. PhD. Eng. Phys. Luminița MORARU** Director of the Doctoral School of Mechanical and Industrial Engineering, "Dunarea de Jos" University of Galati
Scientific referrers,	**Prof. PhD. Eng. Neculai Eugen Seghedin,** "Gheorghe Asachi" Technical University of Iași **Prof. PhD. Eng. Cătălin Amza,** Polytechnic University of Bucharest **Prof. PhD. Eng. habil. Antoaneta ENE,** "Dunarea de Jos" University of Galati

Series I 4: Industrial Engineering, No. 90
GALAȚI,
2023

Leader : Partner :

UNIVERSITAS
GALATIENSIS

The PhD thesis series publicly presented in UDJG since October 1, 2013 are:

Major field ENGINEERING SCIENCES

Series I 1:	**Biotechnologies**
Series I 2:	**Computers and Information Technology**
Series I 3:	**Electrical Engineering**
Series I 4:	**Industrial Engineering**
Series I 5:	**Materials Engineering**
Series I 6:	**Mechanical Engineering**
Series I 7:	**Food Engineering**
Series I 8:	**Systems Engineering**
Series I 9:	**Engineering and management in agriculture and rural development**

Major field SOCIAL SCIENCES

Series E 1:	**Economics**
Series E 2:	**Management**
Series E 3:	**Marketing**
Series SSEF:	**Sports science and physical education**

Major field HUMANITIES

Series U 1:	**Philology - English**
Series U 2:	**Philology - Romanian**
Series U 3:	**History**
Series U 4:	**Philology – French**
Series SJ:	**Law**

Major field MATHEMATICS AND NATURAL SCIENCES

Series C:	**Chemistry**

Major field BIOMEDICAL SCIENCES

Series M:	**Medicine**
Series F:	**Pharmacy**

Acknowledgments

This thesis is to all the efforts and collaborations that took place for the result of the PhD years.

My thanks go first of all to Mrs. Prof. Ph.D. Eng. Phys. Luminița Moraru, the scientific coordinator of this work, for the guidance, support, help, patience, trust, granted during the entire process of research and writing of the thesis. I am grateful that I was accepted to be part of the teacher's team, that she provided me with a model of high professionalism, encouraging me to overcome my limits. I really appreciate the time and effort invested in me.

Also, I would like to thank Prof. Dr. Simona Moldovanu for her support, help, significant contribution to my academic success.

I would like to thank all the members of the doctoral committee, Prof. Dr. Eng. Eugen-Victor-Cristian Rusu, Corresponding Member of the Romanian Academy, Prof. Dr. Eng. Antoaneta Ene, Prof. Dr. Simona Moldovanu for the patience with which they analyzed the present work as well as for the suggestions made.

I would like to thank the management of the Department of Computers and Informatics, the management of the Faculty of Sciences and Environment of "Dunărea de Jos" University of Galati for the support shown throughout the research activity.

I would like to thank my PhD colleague, Eng. Felicia Damian for her constant support and encouragement.

Last but not least, I would like to thank the families for their unconditional and constant support during this process.

Galați, 2023   Toporaș (Pană) Lenuța

This summary contains a synthesis of the most eloquent experimental results obtained from theoretical and practical research.

The chapter headings, sub-chapters, figures, tables and bibliographical references are identical to those of the PhD thesis.

Eng. Toporaș (Pană) Lenuța - *Applications of DWI and DTI scanning techniques for rapid assessment of specific parameter changes in brain disease*

Contents

Contents

Eng. Toporaș (Pană) Lenuța - *Applications of DWI and DTI scanning techniques for rapid assessment of specific parameter changes in brain disease*

Contents

Eng. Toporaș (Pană) Lenuța - *Applications of DWI and DTI scanning techniques for rapid assessment of specific parameter changes in brain disease*

Introduction

Introduction

In recent decades, increased life expectancy has resulted in an aging population, which has, in turn, led to a higher prevalence of neurological and brain diseases.

The brain, being the most complex organ and the center of the nervous system, plays a crucial role in our health. Conditions that affect the brain can impair memory, attention span, mood, and motor skills, significantly impacting patients, their well-being, and their families. Common conditions include Alzheimer's, various types of dementia, Parkinson's, multiple sclerosis (MS), Huntington's, and others. Brain tumors can be benign or malignant, and accurately detecting and measuring the tumor is essential for diagnosis. Tumor growth can put pressure on the brain and cause irreversible damage. Imaging techniques are commonly used to detect brain tumors, with advancements in science leading to improved medical imaging.

Magnetic resonance imaging (MRI) is a widely used imaging technique for diagnosing brain-related issues. In contrast to computerized tomography (CT) scans or X-rays, MRIs do not use radiation and are relatively non-invasive and efficient for in vivo diagnosis. Advancements in hardware and software have contributed to reduced MRI scanning times and improved image quality and accuracy. MRI scans help visualize brain tissue anatomy and brain activity, aiding in the diagnosis and monitoring of treatment plans for patients.

MR image analysis is typically performed by a radiologist, making the analysis directly influenced by the individual's experience and training. Due to image acquisition, inherent noise, tissue shading, and variations in conditions, MR image analysis remains a research challenge.

In this thesis, we examine MRIs obtained through diffusion-weighted imaging (DWI) and diffusion tensor imaging (DTI) techniques from public and private databases of both healthy individuals and those with brain conditions.

The images were processed using MatlabR2018a and ImageJ to create a 3D representation of the brain and tumors. Additionally, MedCalc, a biomedical research software, was utilized to interpret the results.

Motivation

Brain research demands an interdisciplinary approach, with technological advancements continuously expanding the field's boundaries. Modern MRI analysis can be achieved using various methods and algorithms found in research papers, journals, textbooks, and conference papers, as well as employing diverse imaging techniques like DWI, DTI, or different statistical weightings.

The aims of this scientific study

The primary goal of this scientific research is to analyze MR brain images obtained using DTI and DWI techniques by employing pre-processing, advanced processing, and post-processing methods, while monitoring changes in their defining parameters.
The main objectives include:
-   enhancing the spatial quality of brain MR images,
-   comparing the performance of segmentation algorithms,

Eng. Toporaș (Pană) Lenuța - *Applications of DWI and DTI scanning techniques for rapid assessment of specific parameter changes in brain disease*

Introduction

- identifying basic texture primitives to differentiate brain lesions,
- 3D reconstruction and analysis of MR brain images.

To accomplish these goals, we have utilized various preprocessing methods such as bilateral filter, anisotropic diffusion filter, maximum and minimum filter, neural network filter, and median filter on brain images of patients with different brain disorders. Additionally, we have employed 3D reconstruction and analysis of healthy brain MR images, as well as for subjects with strokes, multiple sclerosis, and gliomas.

Chapter 1- Current insights into imaging processing outcomes to the brain diseases

The brain, serving as the central component of the nervous system, comprises billions of nerve cells, each consisting of neurons that process and convey information via electrical and chemical signals. These signals facilitate communication between various parts of the brain as well as between the brain and different regions of the body [1]. Mental health is an essential aspect of an individual's capacity to think, experience emotions, engage with others, earn a living, and enjoy life [2]. Symptoms in individuals with brain conditions vary based on the nature of the condition. The number of people affected by neurodegenerative diseases is estimated to reach 65.7 million by 2030, with a threefold increase by 2050 [3]. Neurodegenerative diseases damage brain tissue and nerves, resulting in altered personalities and confusion in patients. The development of most neurodegenerative conditions is attributed to a combination of genetic and environmental factors, hindering the prediction of those who may develop such diseases. While some neurodegenerative disorders primarily lead to movement difficulties, others predominantly cause cognitive impairments (dementia). The most common neurodegenerative diseases include Alzheimer's disease, Parkinson's disease, multiple sclerosis (MS), motor neuron disease or amyotrophic lateral sclerosis, and Huntington's disease.

1.1. Medical imaging

Medical imaging methods and techniques can be categorized as follows [18]:
- ➢ Computed tomography, which combines computer technology with X-rays;
- ➢ Nuclear imaging, with primary techniques including single photon emission tomography (SPECT) and positron emission tomography (PET);
- ➢ Magnetic resonance imaging (MRI);
- ➢ Ultrasound imaging.

MRI examination is favored over other imaging techniques, such as X-rays, computed tomography (CT), and ultrasound, for acquiring high-contrast medical images. MRI parameters, including T1, contrast T1, T2-weighted, FLAIR, and PD (proton density), are commonly employed in the detection and diagnosis of various neurological disorders, including stroke, cysts, tumors, Parkinson's disease, and Alzheimer's disease [19]. Magnetic resonance imaging or diffusion-weighted imaging (DWI) appears to be more sensitive than CT for the early detection of ischemic stroke [20].

1.2. MRI acquisition

Image registration is a crucial step in imaging, representing the ability to geometrically align one dataset with another for multimodal image mapping, atlas construction, arithmetic operations on images (averaging, subtraction, correlation), and 3D reconstruction [23]. Medical image registration methods can be classified as follows: by information type (landmark-based methods and image intensity-based methods), based on image dimensions (2D-2D, 3D-3D), based on transformation (rigid and non-rigid registration), and depending on the image sources (monomodal and multimodal) [24]. As a valuable tool in automated diagnostic algorithms, medical image registration enables the analysis of T2w and DTI MR images in the same coordinate system, eliminating or correcting artifacts induced by patient movement during image acquisition

[30]. Zhang et al. employed mutual information (MI) for image registration in multimodal applications [28]. The common histogram is utilized in calculating the mutual information between two images using interpolation methods. MI is a robust technique for matching multimodal images based on their intensities.

1.3. Skull stripping methods

Raw brain MRI images contain elements such as eyeballs, skin and bone tissue, fat, and muscles. These components can be automatically removed. Generally, the precise extraction of brain regions results in a brain mask by eliminating non-cerebral tissues [35]. Most extraction methods are validated on T1-weighted images, as they provide exceptional contrast between brain tissues [36].

1.4. Filtering methods

Useful information from MR brain images can be compromised by noise or other artifacts that may appear during the acquisition process, due to the technology employed and/or the positioning and movements of the patient. Noise can also be introduced as a result of transmission and compression errors in digital MR images, making noise removal the first step before analyzing the images [42]. Most natural images contain additive random noise, which is modeled as Gaussian noise [43], Poisson noise, or salt and pepper noise. Generally, MR brain images are affected by Rician-type noise [2, 44]. The application of filters leads to improvements in the quality of the generated images, in terms of both resolution and peak signal-to-noise ratio (PSNR) [49], while preserving edges and fine details within the images [50]. Broadly, filters as noise removal tools can be divided into two main categories: linear and non-linear [51].

1.5. Segmentation methods

Segmentation is a crucial step in image analysis and interpretation, defined as the delineation of anatomical structures and other regions of interest. Accurate segmentation of MR brain images involves separating brain tissues, such as gray matter, white matter, and cerebrospinal fluid or various tumors. Segmentation can be performed on both 2D MR images (pixel processing) and 3D MR images (voxel processing) [65, 69].

A simple method for brain tissue segmentation can be achieved through thresholding, using the gray level intensity histogram to determine the optimal pixel intensity values that separate the desired brain tissue classes. However, this technique does not consider the spatial characteristics of an image and may result in misclassification due to random noise and the complexity of the intensity distribution of brain tissues [71]. Somasundaram et al. [78] classified WM, GM, and CSF brain tissues using k-means and Fuzzy C-Means segmentation methods from T1w and T2w MR images for healthy patients. They demonstrated that WM was correctly classified by both methods, but the Fuzzy C-Means method misclassified GM and CSF.

The region-growing-based segmentation method was used by Park and Lee [79]. Utilizing a mask created through morphological operations, they identified two "seed" regions placed in the cerebral regions and the non-cerebral regions. These regions expand or grow and are used in the process of removing non-cerebral/scalp regions from T1w images. A novel hybrid approach is achieved by combining the watershed method with the edge detection method using the Canny operator. The method proposed by Shah [80] was employed to detect tumor boundaries. The results showed that this combination can provide effective tumor extraction from MR images and is an improvement over the watershed method. Mehmood et al. [87] developed a new neural

network (the Siamese convolutional neural network) to improve the classification of Alzheimer's disease in various stages (no dementia, very mild dementia, mild dementia, and moderate Alzheimer's) using MRI. The images were segmented using the K-means algorithm, targeting the extraction of different pixel intensities belonging to WM, GM, and CSF. Subsequently, the neural network was employed to accurately classify the disease stages. An exceptional test set accuracy of 99.05% was achieved for dementia stage classification. The proposed approach offers an accuracy improvement of 3% over the 3D convolutional network and up to 6% for multiclass classification.

1.6. Statistical texture analysis

Numerous approaches have been proposed to quantify and characterize the texture of MR brain images. This section will detail some of them.

Harrison et al. [89] investigated texture in MRI brain datasets of multiple sclerosis patients, to classify the white matter and multiple sclerosis lesions. Texture analysis was performed using MaZda software, which separates image regions corresponding to multiple sclerosis plaques and white matter (WM) or normal-appearing WM regions with a very high accuracy of 96%–100%. Zhang et al. [91] examined the 3D textural features in specific regions of interest (ROIs) for T1w brain images as a potential Alzheimer's disease screening tool. Comparative analysis was performed on image sets belonging to both diseased and healthy patients. ROIs containing cerebrospinal fluid (CSF) had higher classification accuracy, ranging from 64.3% to 96.4%. Vidyarthi and Mittal [95] analyzed texture on a T1w dataset containing five different types of malignant tumors using the texture co-occurrence matrix method (TOM Texture Co-occurrence Matrix). Two matrices of texture on filtered images with high-pass filter and low-pass filter were generated. TOM extracts spatial features and static features, and the algorithm's performance is validated by the t-test statistic. Experimental results suggested that this method allows for better textural analysis compared to the gray level co-occurrence matrix (GLCM) and run length matrix (RLM). Texture analysis using GLCM to classify ALS and healthy patients from T2w images was employed by Ishaque et al. [99]. The classification performance of the proposed method depends on the image resolution.

1.7. Morphological operations

Shattuck et al. [101] used morphological operations such as erosion and dilation for processing T1w images to isolate and classify brain tissues. Sharma et al. [102] employed erosion and dilation as morphological operations in the preprocessing stage of MR images for patients diagnosed with grade I-IV glioma, facilitating the detection and segmentation of brain tumors. Bava and Shahan [103] performed segmentation of noise-corrupted and binarized MR images using opening and closing morphological operations, utilizing a multi-structure element (multiple structure elements in the same window). Tumor tissue segmentation followed. Dilation and erosion were used by Akram et al. [104] to remove pixels resulting from the segmentation operation of brain tumors. Some morphological operations, such as opening, hit-or-miss, erosion, closure, and reconstruction, in pre- and post-processing stages for tissue extraction from brain images were used in [108]. Gandhi et al. [109] investigated erosion, dilation, opening, closing, and averaging as filtering methods and morphological operations in MR brain image processing. They found that erosion and opening performed best in removing Gaussian noise.

1.8.   Fractal geometry for image analysis

Another approach in the analysis and detection of specific properties of brain tissues, brain disorders, or the analysis of the complexity of brain structures is represented by fractal geometry.

Esteban et al. [113] compared T1w and T2w images of healthy patients and patients presenting with multiple sclerosis lesions. Fractal dimension was used to determine gray matter abnormalities. Jayasuriya et al. [114] reported a novel approach capable of identifying symmetry in brain structures using the mid-sagittal plane for 3D MR images. They employed concepts of fractal dimension and lacunarity. For images that display severe asymmetry due to tumors or neurological damage, the accuracy of the mid-sagittal plane position may be affected, and the study may no longer demonstrate the expected efficacy. Di Ieva et al. [117] also evaluated intra-tumoral structures and brain gliomas of different grades using Susceptibility-weighted imaging (SWI) brain MR images through fractal analysis. The results indicated that the mean value of the fractal dimension for grade II gliomas was 1.682 ± 0.278 and for grade IV gliomas was 2.247 ± 0.358. The authors demonstrated that fractal analysis can differentiate glial tumor grades. Jiménez et al. [118] designed a web platform for the calculation and analysis of fractal dimension in 3D brain MR images of healthy, multiple sclerosis, and Alzheimer's disease patients. The platform allows interactive 3D visualization of the analyzed volumetric data. The results showed a significant decrease in the 3D fractal dimension of the gray matter in both normal aging and Alzheimer's disease, while in patients with multiple sclerosis, an increase in the value of the 3D fractal dimension specific to the gray matter was found compared to healthy subjects. Hoyos et al. [123] analyzed T1w images containing primary tumors and their growth dynamics. The *in vivo* evolution of 3D tumors was examined based on the fractal dimension and local roughness of the brain tissue. The authors showed that as the lesion becomes more aggressive, the complexity of the tumor-host interface increases. Kim et al. [124] performed a comparative analysis of 2D and 3D fractal features in classifying meningioma grades from DTI images. The 3D fractal model outperformed the 2D fractal model in tumor classification.

1.9.   Edge detection

Edges present in medical images have a significant impact on the early detection of brain disorders, classification of malformations, and serve as an essential adjunct to diagnosis [125]. Rulaningtyas et al. [126] proposed three methods based on first-order derivative operators, Robert, Prewitt, and Sobel, for edge detection. The results showed that the Sobel operator is the most suitable for segmenting brain tumor edges. Edge detection based on first-order (gradient method) and second-order (Laplacian operator) derivative operators were used by Mamta and Parvinder [127]. They demonstrated that the Canny method allows the detection of both strong and weak edges. Somasundaram et al. [128] use first-order derivative-based operators to determine edges from T2w brain images used in the non-cranial tissue removal algorithm. Diwakar et al. [130] analyzed and presented the advantages and disadvantages of classical edge detection techniques using Robert, Sobel, Prewitt, Marr-Hildreth, and Canny type operators. They proposed a method for detecting continuous, well-defined, and localized edges called Cellular Automata. The method was used to detect the edges of cancer cells present in brain tissues. Kalaiselvi et al. [132] proposed a hybrid edge detection method by combining contrast enhancement of T2w brain images and generating an edge indication map. In the map generation, the Roberts, Sobel, Prewitt, Canny, and Marr-Hildreth operators were used, selecting the pixels that belonged to the edges present in the images. The method generates continuous edges and removes the false edge pixels. For edge detection, Matkar and Borse [136] used the active

Eng. Toporaş (Pană) Lenuţa – *Applications of DWI and DTI scanning techniques for rapid assessment of specific parameter changes in brain disease*

Chapter 1- Current insights into imaging processing outcomes to the brain diseases

contour method and compared it with traditional methods (Sobel, Canny, and Prewitt). The active contour method resulted in better accuracy for image segmentation.

1.10. Skeleton operations

Object contours refined using the skeletonization technique have a wide variety of uses and applications in virtual navigation, virtual endoscopy and animation, segmentation of anatomical structures, medical image registration, 3D object matching, morphology, and surface reconstruction [118].

Cubon et al. [137] studied the fractional anisotropy parameters and average diffusivity of the white matter (WM) skeleton using tract-based spatial statistics (TBSS) in DTI brain images of concussed patients. The mean diffusivity values were higher in patients who had concussions in the left hemisphere, and it was more sensitive to the determination of mild injuries. In contrast, the fractional anisotropy parameter was more sensitive to the investigation of more severe lesions. WM skeletonization was used by Kolind et al. [138] to study diffuse and global myelin loss in the brains of patients with primary progressive multiple sclerosis. The authors demonstrated that the myelin water fraction was diffusely reduced throughout the white matter skeleton in diseased patients. Lopez et al. [118] binarized 3D MR brain images to generate a 3D skeleton, using a web platform. The web platform can simultaneously perform fractal dimension (FD) computation on multiple images with multiple thresholds, both on their original and skeletonized representations. This approach allows for a more comprehensive analysis of brain structures and their complexity, contributing to the understanding and diagnosis of various neurological conditions.

1.11. Similarity analysis of brain areas in MR images

Asymmetries in MR brain images are rendered by means of internal structural networks, cortical morphometry, or symmetry between hemispheres. To examine symmetries/asymmetries, there are two general approaches: point-to-point comparisons between left and right hemispheres and the use of sulcal boundaries to separate regions within each hemisphere [141]. Automatic MR image processing techniques have allowed the analysis of differences and similarities between the two cerebral hemispheres to detect various anomalies and/or differences in anatomical structures. The analysis of brain symmetry is based on the determination of the average sagittal plane [142]. Somasundaram and Kalaiselv [143] used bilateral symmetry of the human brain using T2w images of healthy and single-hemisphere tumors. They measured the vertical symmetry of the cerebrospinal fluid (CSF) between the two hemispheres based on the fuzzy symmetric measure, classifying the images from databases containing brain images with healthy structures and pathologies. Ruppert et al. [144] determined the symmetry between the two hemispheres based on edge features extracted with the Sobel 3D operator. Shah and Chauhan [145] delineate the two hemispheres based on the Bhattacharya coefficient. They can also be delimited based on the concepts of fractal dimension and lacunarity analysis or by measuring the Kullback–Leibler coefficient [146]. Moraru et al. [148] analyzed the structural similarity index (SSIM) by evaluating the structural similarity of a processed image relative to a reference image. MR images of patients diagnosed with cerebrovascular disease (fatal stroke and subacute stroke); neurodegenerative diseases (Alzheimer and Pick); inflammatory or infectious diseases (multiple sclerosis); and brain tumor (meningioma) were used. Inter-hemispheric brain similarity in patients with neurodegenerative diseases (Alzheimer, Huntington, Pick) and healthy patients was analyzed by Moraru et al. [149]. In the study, starting from the

SSIM similarity index, ESSIM (the similarity index for the edges of an image) and the FSSIM (feature similarity index between two images) are defined. By using feature images, structural similarity indices, and based on multicollinearity analysis, structural differences between MR brain images affected by the natural aging process and those affected by neurodegenerative diseases can be detected. The Jaccard similarity coefficient was used by Zanaty [151] to study the similarity between seed region growing segmentation and manual segmentation using T1w brain images. An average segmentation score of 90% was obtained with a noise level of 9–3%. Davarpanah and Liew [154] used lacunarity to extract an initial plane of symmetry from 3D T1w, T2w, PD, simulated/artificial, and real images. The fractal dimension was used to determine the degree of similarity between the two hemispheres by analyzing a stack of images consisting of axial images. Experiments have shown that the estimated mean sagittal plane is accurate and is independent of the noise level.

1.12. 3D brain reconstruction from 2D MR images

2D and 3D brain imaging is used to visualize anatomical and pathological components (tumors, brain surface, skull, arteries, and veins). Nowadays, surgeons require a clear and precise 3D image of the brain during complex robotic operations [68].

Chiorean et al. [155] address the 3D reconstruction of the pathological area from DICOM brain images combined with a 3D reconstruction from the segmented images and viewing both volumes in the same window. Using a neurosurgical planning software, Mert et al. [156] used a 3D brain surface visualization technique obtained from 2D MR brain images. Topographic localization of the lesions was accurate and fast compared to 2D images. Tumor extraction from 2D T1w brain images is also performed by Ali et al. [157]. To be rendered into 3D images, the tumor was extracted from the 2D T1w images using morphological opening operation. Arakeri et al. [158] proposed 3D reconstruction and quantification of brain tumor volumes from 2D MR images. The tumor surface is constructed based on the marching cubes (MC) algorithm. The volume is calculated taking into account the gap between the slices, the area of the tumor on each slice, and the thickness of the slice. The results obtained generated a precise 3D model in a short time. Harput et al. [159] performed a 3D brain surface reconstruction from 2D T1w brain images from patients with neocortical lesions using a free software called OsiriX. Their method allowed the precise identification of tumor boundaries. The detection of the tumor and its 3D reconstruction by the "seeded region growing" technique was carried out by Lopes et al. [160] using 2D T2w image sets. Zahira et al. [162] propose tumor rendering from MR brain images using ImageJ software tools. This software loads multiple stacks of 2D images in one window and allows analysis, editing, and display in 3D. Their proposed study uses 2D images and has the following steps: preprocessing, segmentation, feature extraction, feature selection, classification, and 3D reconstruction.

Chapter 2 - Mathematical methods and models for assessing imaging parameters in research

2.1. Magnetic resonance imaging

The phenomenon of magnetic resonance in molecular beams was initially elucidated by the eminent physicist Isidor Isaac Rabi, who was subsequently awarded the Nobel Prize in 1944 for his groundbreaking work. Subsequent investigations into magnetic resonance in solids and liquids by Felix Bloch and Edward Purcell garnered them a shared Nobel Prize in 1952. Primarily, magnetic resonance was employed for the abiotic analysis of atomic and molecular structures.

A pivotal discovery in 1971 revealed a discernible difference between the relaxation times of healthy and tumorous tissues. This finding was instrumental in the advancement of magnetic resonance imaging (MRI) technology for human imaging applications. R. Damadian played a significant role in the development of this technology, demonstrating that tumors and normal tissue could be accurately differentiated using MRI techniques.

2.1.1. MRI (T1, T2, PD)

The images acquisition through the MRI technique are grayscale, reflecting the concentration of hydrogen within each tissue. Cirnici [169] expounded upon the fundamental principles of nuclear magnetic resonance (NMR) operation, focusing on the behavior of hydrogen atoms, or protons, within a magnetic field. In the human body, the prevalence of fat and water is high, and both contain numerous hydrogen atoms, which facilitates the acquisition of MR images [170]. The hydrogen atom comprises a single electron (the neutron possesses no electric charge) that orbits the nucleus, which consists of a single proton. The proton exhibits the property of spin, that is, rotation around its own axis, generating both a magnetic moment (due to the electric charge) and a kinetic moment (attributable to the proton's mass). The spin values for the proton, electron, and neutron are equal to $-1/2$ and the spin of atoms is always a multiple of $+1/2$. For a hydrogen atom, the spin value is $1/2$, and the nuclear spin assumes the value of 1. In the absence of an external magnetic field, also known as a static magnetic field (b_0), the magnetic moments (spins) of biological tissues are oriented chaotically [168].
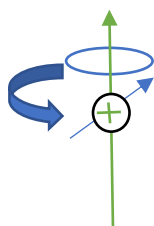
Figure 2.1 Interaction between the proton and the static magnetic field b_0

Under the influence of a static magnetic field b_0, atoms reorient themselves due to the magnetic polarity of the spin. Consequently, half of the atoms align with the magnetic field b_0 in a north-north configuration, while the other half align in a north-south configuration [168]. In addition, the proton exhibits a precession movement as a result of its spin, which entails the movement of the proton's spin axis around the external magnetic field b_0. The application of magnetic pulses at Larmor resonance frequencies (magnetic field denoted by b_1, perpendicular to b_0) induces a reversion in the orientation of tissue proton spins, leading to variations in their orientation or

phase. The alignment of protons occurs rapidly, resulting in the magnetization of the tissue (Figure 2.2).

<div align="center">(a)   (b)</div>
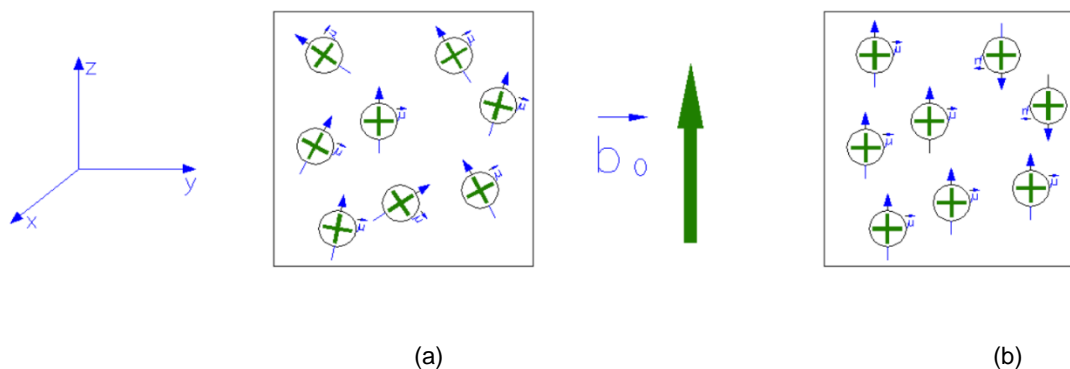
Figure 2.2 Examples of hydrogen atom spin orientations: (a) in the absence of magnetic field b_0; (b) in the presence of magnetic field b_0

During this process, an absorption and exchange of energy occurs, giving rise to the phenomenon of resonance. To transform the information provided by the resonance frequencies into intensity level-correlated data, the Fourier transform is utilized. Intensity levels are represented in shades of gray within a pixel matrix. Consequently, the perturbances associated with various conditions in the human body are visible in MR images [168, 170]. Following this brief event, the spins relax by returning to their initial states. There are two types of spin relaxation processes: longitudinal relaxation, characterized by the time constant T1 (the time required for 63% of the longitudinal magnetization energy to be recovered in the tissue), and transverse relaxation, characterized by the time constant T2 (the time required for 63% of the transverse magnetization to be lost, leaving 37%) [171]. The MRI receiver detects these changes, and the obtained information is processed by a computer to generate MR images. The gray levels in the images are dependent on the T1 and T2 relaxation times, as well as the number of protons present in the tissues, which varies from one tissue to another. Short T1 tissues appear bright (e.g., fat, white matter), while long T1 tissues appear dark (e.g., cerebrospinal fluid, CSF). Tissues with short T2 values are dark (e.g., white matter), whereas those with long T2 values (e.g., CSF and urine) are bright. To differentiate tissues based on these relaxation times, MR images can be weighted [173].

The scan parameters for MR images include TR (repetition time) and TE (echo time), where TR > TE. TR is defined as the time interval between successive sequences of pulses applied to the same slice, while TE represents the time between the application of the resonant pulse and the receipt of the echo signal. A T1-weighted image is obtained when both TE and TR are short. This type of image is utilized to analyze the cerebral cortex, identify fatty tissue, characterize focal liver lesions, obtain morphological information, and examine blood (methemoglobin), protein liquid, certain forms of calcium, and melanin. A T2-weighted image is obtained when both TE and TR are long. This imaging modality is employed to detect human brain white matter lesions, demyelination and axonal loss, cysts, joint fluid, and pathological conditions that cause increased extracellular fluid (sources of infection or inflammation), all of which are represented with high intensity [170,174].

A PD-weighted image is obtained when the signal emitted by various tissues corresponds to proton density. Few protons result in a low and dark signal in the PD image, whereas numerous

protons generate a strong signal, rendering the PD image bright [176]. In this type of image, fat appears with high intensity.

2.1.2. DWI

Diffusion-weighted imaging (DWI) is a technique specific to MRI, which is based on the diffusion of water molecules [177]. Diffusion, also known as Brownian motion of gas or liquid molecules, is induced by intermolecular interactions. In a homogeneous medium, diffusion is random and isotropic. Brownian motion was discovered in 1828 by botanist Robert Brown while he studied the motion of microscopic pollen particles suspended in a liquid [178]. Diffusion is a phenomenon wherein molecules are randomly transported over time from one spatial location to others. Einstein's diffusion equation in three dimensions is provided in [179].

$$D = \frac{<\Delta r^2>}{2n\Delta t} \tag{1}$$

In this equation, D represents the diffusion coefficient (in mm²/s), r denotes the mean square displacement of the molecules, n signifies the concentration of the molecules, and Δt corresponds to the diffusion time.

The human body, when sequentially scanned using the DWI technique, yields 3D stacks of volumes corresponding to their sensitization gradient. For each DWI image, the diffusion parameters of water are measured in a specific direction by sensitizing it with a magnetic field. Water diffusivity in human body tissues is determined by applying diffusion sensitization gradients to T2-weighted spin-echo sequences. The scalar quantity characterizing diffusion sensitization is referred to as the b-factor, expressed in s/mm². In the DWI technique, the b-factor depends on the presence of a gradient magnetic field, the tissue's diffusion factor, and the diffusion time. The gradient field is employed to amplify the effects of diffusion in a particular instantaneous direction, resulting in an increased b-factor. Dark areas, defined as a map of the diffusion coefficient, are observed in cases of infection, neoplasia, inflammation, and ischemia [177].

2.1.3. DTI

Diffusion tensor imaging (DTI) is a specialized type of diffusion in MRI imaging, introduced in 1994 by Basser, Mattiello, and LeBihan [185]. DTI is an MRI technique that measures anisotropic water diffusion at the cellular level and allows for *in vivo* visualization of white matter tracts. DTI provides valuable information about the geometric and microstructural organization of white matter. In recent years, the methods of action and DTI analysis have evolved, continuously improving the precision of diffusion tensor measurements, spatial resolution and accuracy, and the reduction of artifacts caused by the diffusion process. DTI has become a technique that offers insights into brain maturation and neurodegenerative disorders. The diffusion tensor, denoted by D, is defined as follows [184]:

$$D = \begin{bmatrix} D_{xx} & D_{xy} & D_{xz} \\ D_{yx} & D_{yy} & D_{yz} \\ D_{zx} & D_{zy} & D_{zz} \end{bmatrix} \tag{4}$$

The diagonal elements D_{ii} represent the diffusion along the x, y, z axes, while the off-diagonal elements are symmetric and act as covariance terms. These terms contribute to the calculation of three groups of vectors called eigenvectors λ_1, λ_2, λ_3. The eigenvectors indicate the direction of scalar diffusion at each point defined by the diffusion tensor, resulting in the formation of a three-dimensional ellipsoid (Figure 2.3).
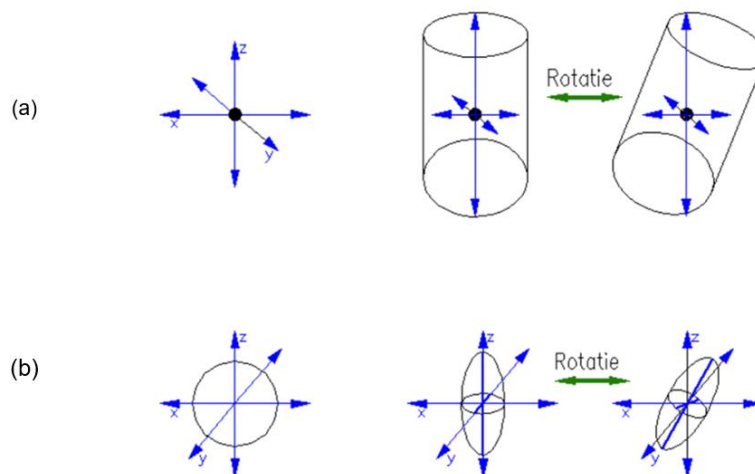

Figure 2.3 Schematic representation of diffusion: (a) isotropic, (b) anisotropic

Diffusion is considered as being isotropic (Figure 2.3(a)) when $\lambda_1 \approx \lambda_2 \approx \lambda_3$ and anisotropic (Fgure 2.3(b)) when $\lambda_1 > \lambda_2 > \lambda_3$. Diffusion in white matter regions is anisotropic, while in gray matter and cerebrospinal fluid, diffusion is isotropic [184]. Longitudinal diffusion is defined by λ_1, which represents the direction of the axon, whereas perpendicular diffusion is described by λ_2 and λ_3 [186]. The anisotropy properties of the diffusion phenomenon are measured using fractional anisotropy (FA). The parameters employed in characterizing information from DTI images include longitudinal, perpendicular diffusivity, and fractional anisotropy [186,187].

2.2. Textural features

Texture analysis of MR brain images hold significant interest in medical imaging. The texture of the images represents the spatial distribution of the intensity and/or color levels of the pixels within the areas of interest in an MRI brain image.

2.2.1. First-order textural features

The vector associated with the histogram of a digital MR image, which is assimilated with a first-order statistic associated with the gray levels of the pixels in the image, allows the statistical distributions of Skewness and Kurtosis, indices of asymmetry and peakedness, computation [188, 189].

2.2.2. Second-order textural features

Second-order textural features are dedicated to the joint probability occurrence of a pair of gray level values for a pair of randomly placed pixels. The second-order features are computed from the co-occurrence matrix; the output image C_d (i, j) is obtained from an image I with gray levels *i, j*, which are at a distance d [188],

$$C_d(i,j) = \sum x,y \begin{cases} 1, & I(x,y) = i, \quad I(x+dx, y+dy) \\ 0 \end{cases}$$

(8)

d = (dx, dy) denotes the displacement vector.

Entropy (E) and energy (EN) are characteristics related to the order (regularity or homogeneity) of pixels [189]:

$$E = -\sum_{i,j} C_d(i,j) \ln C_d(i,j) \qquad (9)$$

$$EN = \sum_{i,j} C_d(i,j)^2 \qquad (10)$$

2.2.3. Derivative filters for edge detection

For an accurate diagnosis of brain disorders, the edges of brain tissues in MR images are crucial elements for analysis. Edge detection is a complex process that relies on operators that impose convolutions between first-order derivative filters [149], second-order derivative filters [190], the image gradient, and the original MR image. An edge represents the boundary between the object and the background or between objects and is defined by the totality of pixels with sharp discontinuities in gray levels. Edges are determined by analyzing the distribution of pixels in an MR brain image and evaluating the intensities around a fixed pixel. Significant variations in intensity between two regions in the vicinity of a pixel allow it to be classified as belonging to an edge [191, 192].

2.2.3.1. First-order derivative filters

A MR brain image is defined as a two-dimensional function describing the position of a pixel (x, y) and the grayscale intensity value f (x, y) of the pixel at position (x, y). First-order derivative filters utilize the convolution (*) operation. The first-order gradient operators most frequently employed in detecting MRI brain images are the Prewitt, Roberts, and Sobel operators (or filters).

a. Roberts Filter

The operator consists of two 3 * 3 convolution masks, to detect vertical and horizontal directions of the edges in an image [197,198].

b. Sobel filter

The Sobel operator uses two 3 * 3 convolution masks [199] and performs a weighted averaging of pixel intensities through smoothing and derivative operations [200, 201].

c. Prewitt Filter

The Prewitt operator consists of two convolution masks Gx and Gy, of size 3 * 3, which perform convolutions on the original image f (x, y) to calculate approximations of the gradient operator [197]. The Prewitt filter exhibits high performance in edge detection from digital images corrupted with Poisson noise [202].

2.2.3.2. Second-order Derivative Filters

Edge detection in a digital image also relies on the use of the Laplacian operator.

a. The Laplacian Filter

The Laplace operator is computed using the second-order derivative approximations of the function f (x, y) for the gray value of the pixel at position (x, y). This operator is often convolved with an image that has first been smoothed with a Gaussian filter to decrease sensitivity to noise [192]. Areas in the image where the intensity of the gray levels is less than or greater than zero are located in the vicinity of the edge. This operator is noise-sensitive and pixels with sudden changes in intensity can generate double edges.

b. Laplacian of Gaussian (LoG) Filter

The LoG filter is a combination of Laplacian and Gaussian functions employed to find real edges in the image. It tests wider areas around the pixel, and does not fail when the image contains corners and curves. It uses the following three successive operations: filtering with a Gaussian filter; enhancement using a Laplacian operator, and edge detection as a zero crossing in the second derivative for a digital image.

2.2.4. Histogram of Oriented Gradients (HOG)

Histogram of Oriented Gradients (HOG) is used for object detection by counting the number of times a gradient intensity orientation occurs, in a region of the MR image. To obtain the HOG, the image is divided into small contiguous regions, and the gradient orientation histogram is calculated based on the pixels in the regions. Combining histograms represents HOG. To diminish changes in illumination or shadows, local histograms are normalized by determining the intensity measure over larger image regions called blocks [205].

2.2.5. Mutual Information

Mutual Information (MI) is a measure of the informational correlation between the source and target images with intensities p and q, calculated as [206, 207]:

$$(21)$$
$$MI = H(p) + H(q) - H(p,q)$$

$$H(p) = -\sum_i p_i \log p_i; \qquad H(q) = -\sum_j q_j \log q_j; \qquad H(p,q) = -\sum_{i,j} p_{ij} \log p_{ij} \qquad (22)$$

H(p) and *H(q)* are the marginal Shannon entropies calculated as the probability distribution of gray levels. *H (p, q)* represents the common entropy, while p_i and q_j are probabilities of the marginal distribution of HOG. Finally, p_{ij} is the distribution common probability.

2.2.6. Harris Corners

Harris corners are detected using the algorithm developed by Harris and identify points of interest in MR images with the following characteristics [208]: small illumination fluctuations, invariance to rotation, scaling factor changes, and affine transformations, as well as a small number compared to edge features.

2.3. MRI and mathematical morphology

2.3.1 Morphological operators

Mathematical morphology is based on set theory, integral geometry, and an algebraic network [211]. It is used in the processing of digital binary MR images. The stated purpose is to extract information regarding the shape and size of the objects identified in the images by applying some non-linear morphological operators that use structuring elements. Basic morphological operators are dilation and erosion, from which many other complex morphological operations can be derived, such as opening and closing some regions of the studied image [212].

a. Morphological dilation increases the shapes and sizes of the objects in the binarized image, filling the gaps and joining disjoint shapes.

b. Morphological erosion reduces the shapes and sizes of objects in images by eroding their edges.

c. Morphological closure is achieved by dilation followed by erosion. This operation will close the existing gaps or discontinuities in the objects in the digital image.

d. Morphological opening is composed of morphological erosion followed by morphological dilation in a binary image. Thus, pixels from small shapes or sizes that cannot contain the structuring element will be removed**.**

2.3.2 Skeletonization

Skeletonization is a simplified two-dimensional representation of a shape or object in an image [202]. It applies only to binary images and is represented by reducing objects to lines without changing the structure of the image. The morphological operations of erosion "$\ominus$" and opening "$\circ$" are used with a structural element B, and the operation is repeated k times. The process ends when the function of erosion and opening between the set A and the structural element B is non-zero. The equations that define this morphological operation are [211, 214]:

$$S(A) = \bigcup_{k=0}^{k} S_k(A) \tag{30}$$

$$S_k(A) = (A \ominus kB) - (A \ominus kB) \circ B \tag{31}$$

$$(A \ominus kB) = \left(...\left((A \ominus B) \ominus B\right) \ominus ...\right) \ominus B \tag{32}$$

$$k = \max\left\{k | (A \ominus kB) \neq \varnothing\right\} \tag{33}$$

We have denoted by k the last iterative step before A erodes into the empty object (erosion takes place until the step where if it were repeated one more time, the objects would blend into the background, i.e., there would be no object). The dilation of A is performed with the morphological dilation operation "$\oplus$" and the structural element B, repeating the operation k times. Morphological dilation reconstructs the shape of the skeleton:

$$A = \bigcup_{k=0}^{k} \left(S_k(A) \oplus kB\right) \tag{34}$$

We noted with $S_k(A) \oplus kB$ the dilations by k times, defined as [211, 215]:

$$\left(S_k(A) \oplus kB\right) = \left(...\left(\left(S_k(A) \oplus kB\right) \oplus B\right) \oplus ...\right) \oplus B \tag{35}$$

The structuring element B is chosen according to the purpose of skeletonization. Skeletonization of an image is sensitive to the noises contained in the image.

2.3.3. Hit-or-Miss Transformation

The hit-or-miss transformation finds particular foreground pixel patterns and assumes a morphological erosion with two disjoint structuring elements. The first structuring element *"hit"* is used to determine the location of pixels in the foreground of the image, and the second structuring element *"miss"* determines the location of pixels in its background. The hit-or-miss transformation is useful for identifying specific patterns in an image, such as corners or other features.

2.4. Statistical elements, quality metrics and clustering methods

2.4.1. Peak Signal-to-Noise Ratio (PSNR)

PSNR is a widely used metric for evaluating the performance of noise removal methods in MR images [218]. PSNR is defined as the ratio of the maximum possible power of a signal to

the power of the noise affecting its fidelity, expressed in decibels [69]. A high PSNR value indicates better MR image reconstruction quality quantitatively.

2.4.2. Pearson correlation coefficient

The Pearson correlation coefficient is used to highlight the relationships and associations that exist between two methods. For two variables x and y, with n studied samples, it is defined by [220]:

$$r_{xy} = \frac{\sum_{i=1}^{n}(x_i - \bar{x})(y_i - \bar{y})}{\sqrt{\sum_{i=1}^{n}(x_i - \bar{x})^2}\sqrt{\sum_{i=1}^{n}(y_i - \bar{y})^2}} \qquad \bar{x} = \frac{1}{n}\sum_{i=1}^{n}x_i \qquad \bar{y} = \frac{1}{n}\sum_{i=1}^{n}y_i \qquad (40)$$

where $\bar{x}$ and $\bar{y}$ represent the arithmetic means of the two variables. The Pearson coefficient takes values in the range between −1.0 and +1.0. A positive value indicates that both variables vary in the same direction (both have increasing or both decreasing variation), while a negative value indicates that one variable has a positive increasing variation and the other has a negative variation [221].

2.4.3. SSIM Structural Similarity Index

Brain MR images provide information about brain tissues and potential structural changes that may lead to various neurodegenerative diseases. Wang et al. [222] proposed the Structural Similarity Index (SSIM) to study image quality. SSIM takes into account and conducts a comparative analysis of the luminance, contrast, and structure of a pair of images.

To define this metric, the luminance *l (x, y)*, contrast *c (x, y)*, and structure *s (x, y)* of two digital images, denoted as x and y, each with dimensions N x N, were considered. The three components are independent, which means that changing the contrast or brightness does not affect the image structures. The SSIM for two binarized images *x* and *y* is [222, 224]:

$$SSIM(x,y) = \left[l(x,y) \right]^{\alpha} \left[c(x,y) \right]^{\beta} \left[s(x,y) \right]^{\gamma} \qquad (41)$$

The powers α, β, and γ are used to adjust the relative importance of each individual component. The similarity index has the following properties: *s (x, y) = s (y, x)*, *s (x, y) ≤ 1*, and *s (x, y) = 1* if the two images are identical. The SSIM index value ranges between 0 and 1 [222, 224].

2.4.4. Dice and Jaccard indices

Let H_1 represent the region of interest in the first binary image and H_2 represent the region of interest in the second binary image [225]. The Jaccard index is given by the relation:

$$J(H_1, H_2) = \frac{|H_1 \cap H_2|}{|H_1 \cup H_2|} \qquad (46)$$

The Dice index is a similarity index calculated as the ratio between twice the intersection and the sum of two binary images. Let H_1 represent the region of interest in the first binary image and H_2 represent the region of interest in the second binary image [226]:

$$D(H_1, H_2) = \frac{2|H_1 \cap H_2|}{|H_1| + |H_2|} \qquad (48)$$

Dice coefficient values are in the range 0 to 1 [227].

2.4.5. Silhouette method

The silhouette method is used for clustering validation and assessing the quality of clustering. The interpretation of clustering results is performed using silhouette plots, which are independent of the clustering algorithm used and based solely on the actual partition of the "objects." The method calculates the silhouette of an object S(i), the average silhouette of a cluster, and the global average silhouette. This index indicates how well a cluster is separated from its neighboring clusters. By calculating the silhouette, one can evaluate the validity of a cluster and determine the correct number of clusters. The Silhouette of object i, S(i), is given by the relation [186, 197]:

$$S(i) = \frac{b(i) - a(i)}{\max\{a(i), b(i)\}} \tag{50}$$

where a(i) represents the average distance of object i from the rest of the objects in the same cluster; b(i) represents the average distance of object i with respect to the objects in the closest cluster. As -1 ≤ S(i) ≤ 1, if S(i) is close to 1, then the object is well classified, and if S(i) is close to −1, then the object is misclassified.

If the structure contains k clusters, the global average silhouette is denoted by S(k). The global average silhouette can be used to decide on the "best" number of clusters: that k for which S(k) is maximum will be chosen. The Silhouette Coefficient (SC) is defined by:

$$SC = \max_k S(k) \tag{51}$$

The Silhouette Coefficient has a strong (well-defined) structure if SC ∈ [0.71 - 1.00]; an acceptable structure if SC ∈ [0.51 - 0.70], and a poor structure if SC ∈ [0.26 - 0.50]. If the value of the SC coefficient ⩽ 0.25, the determined structure is considered artificial [196].

2.4.6. ROC curve

The ROC (Receiver Operating Characteristics) curve has become a statistical standard in the assessment of accuracy for various digital MR image processing techniques (Figure 2.5) [221]. The area under the curve is called AUC (area under the curve). The following interpretations for AUC can be made [228]: AUC = 0, the test classifies incorrectly; AUC = 0.5, random discrimination; AUC < 0.8, the test has limited accuracy; 0.8 ≤ AUC < 0.9, the test has very good accuracy; AUC ≥ 0.9, the test has excellent accuracy; AUC = 1, the test has perfect accuracy.

2.4.7. Bland-Altman method

To estimate the efficiency of methods used in the calculation/evaluation of the same parameter, statistical methods are employed, with the Bland-Altman method being one of the most widely used [229]. The Bland-Altman method evaluates the agreement between two quantitative measurements made using different methods by analyzing the mean, standard deviation, and differences between them. Bland-Altman analysis recommends a limit of agreement within a 95% confidence interval, meaning that the data should fall within ± 2σ of the mean difference between the two measurements. The standard deviation σ is calculated as follows [230, 231]:

$$\sigma = \sqrt{\frac{\sum_{i=1}^{n}(x_i - M)^2}{(n-1)}} \tag{52}$$

where x represents the studied sample, *n* represents the number of studied samples, and *M* is the arithmetic mean of the studied samples.

2.4.8. K-means clustering method

The k-means clustering method aims to identify k classes in the input dataset such that: the data (pixels) within each class are sufficiently similar, and the data from different classes are sufficiently dissimilar [196]. The formal objective function for the K-means algorithm defines the quality of the clustering:

$$J(c_k) = \sum_{x_i \in c_k} \|x_i - \mu_k\|^2 \tag{53}$$

where k represents the number of classes or groups and is a user-chosen input parameter, x_i represents the data point, μ_k represents the centroid for cluster k, and $\|x_i - \mu_k\|$ represents the Euclidean distance between x_i and μ_k. The k-means algorithm seeks to minimize the sum of the squared error across all k groups, according to the relation:

$$J(c_k) = \sum_{k=1}^{K} \sum_{x_i \in c_k} \|x_i - \mu_k\|^2 \tag{54}$$

Since the squared error always decreases with an increase in the number of clusters K, *J(c)* = 0 when K = n, thus, it can only be minimized for a fixed number of clusters.

2.4.9. The Kullback Leibler Divergence

The Kullback-Leibler (D_{KL}) divergence, or relative entropy, is a quasi-metric distance that estimates the difference or similarity between a "true" probability distribution denoted P and an "arbitrary" probability distribution denoted Q. D_{KL} is estimated as follows [200]:

$$D_{KL}(P \| Q) = P \log \frac{P}{Q} \tag{55}$$

If the metric values tend toward zero, the analyzed distributions become more similar [191].

2.5. Fractal dimension

The fractal dimension computation involves determining the self-similarity in an object, where all the elements that make up the object maintain the same aspect but on a smaller scale. MR images are analyzed from the perspective of fractality, considering the distribution of gray level intensities [235, 236]. The box-counting method is an iterative method that, at each step, counts the number of elements dividing the image while respecting the condition that each element contains an irregularity similar to the original object. At each step, the number of elements is denoted by *N*, and the size of the object by *r*, so that the fractal dimension D_f is defined [115]:

$$D_f = \frac{\log N(r)}{\log \frac{1}{r}} \tag{56}$$

The process continues until the smallest element contains the smallest irregularity in the image. The fractal dimension determined by this method can use elements of various shapes (square, triangle, circle, etc.).

2.6. Non-linear filters

Spatial filtering acts on the objects in the initial image, as well as on the pixels in their neighborhood. Spatial filtering has the following advantages [237]:
- ✓ Noise elimination by smoothing impulse-type transitions in the gray level;
- ✓ Preservation of contours, which appear as step-type transitions in the gray level;
- ✓ Speed in performing operations.

2.6.1. Statistical order filters

These filters classify neighboring pixels in an attempt to reduce noise effects while preserving edges. A sliding mask performs certain pixel-by-pixel operations in a filtering algorithm. Local statistics in the neighborhood of the pixel provide the expected value. If the data is ordered (sorted), an order statistic is obtained. A linear combination of the order statistics vector will build an order statistics filter. They are differentiated by how they choose values from the sorted list [238]. The filters used in the study were the minimum and maximum filters. The minimum filter removes salt-type noise, and the maximum filter removes pepper-type noise.

2.6.2. The anisotropic diffusion filters

Recent developments in image processing have led to the emergence of nonlinear filtering techniques that are based on anisotropic diffusion. These techniques have overcome the major drawbacks of conventional spatial filtering and have enabled significant improvements in image quality and enhanced visibility of detected contours. Anisotropic diffusion filtering is a technique that is used for image intensity restoration.

2.6.3. Bilateral filtering

Bilateral filtering is a method for noise reduction and edge preservation by weighting the sum of pixels in a local neighborhood. Each pixel's intensity is replaced by the weighted average of intensity values of its neighboring pixels. The weights have two aspects to consider:
- ✓ the selection of the neighborhood's shape, and the importance given to its neighbors, higher weights are given to closer neighbors;
- ✓ the weights take into account the similarity between the neighboring values and the current value, higher weights are given to similar values.

The weights are normalized to preserve the local average.

2.7. MRI brain volume computation

The brain volume generated from a stack of 2D MR images can be calculated as follows [243]:

$$V = h \times \sum_{k=1}^{m-1} A_k + A_1 \times \frac{\delta}{2} + A_m \times \frac{\delta}{2}$$

(67)

where m is the number of images in the stack; h is the distance between two successive slices in the stack; A_1 and A_m denote the areas of the first and last images in the stack, respectively; A_k represents the area of the kth slice, and δ is the slice's thickness.

Chapter 3 - Original contributions on identifying fundamental texture primitives for brain lesion differentiation

3.1. Brain tissue evaluation based on skeleton shape

In this study, we proposed as a method for detecting edges in the brain structures. A skeletonization algorithm based on morphological mathematical operations (erosion, opening, dilation) is employed. Glioma tumors show a higher heterogeneity and irregularity of tumor tissue and this complex structure qualifies for edge detection and skeletonization as a tool to distingue between tumor area and normal tissue. The proposed method investigates the inter-hemisphere brain tissue similarity of the structures of the cerebral matter. 88 PD and T2w images (256 x 256 pixels), 44 images for patients diagnosed with glioma and 44 for healthy patients we used. The image dataset was downloaded from Harvard's Whole Brain Atlas website for free [246]. Two datasets: D1 contains original raw images affected by Rician noise and D2 consists of the same images pre-processed for noise removal using an anisotropic diffusion filter, are investigated. The flow chart of post-processing and analysis are shown in Figure 3.1.
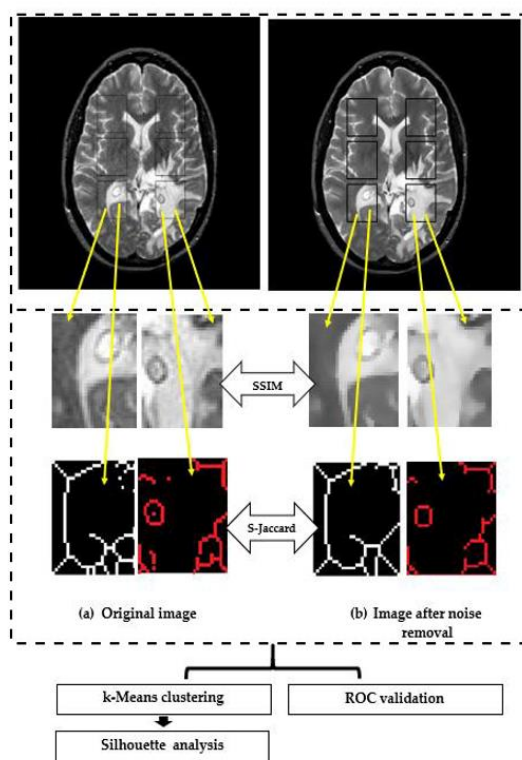
Figure 3.1 Flow chart

A mask in rectangular shape (35 x 45 pixels) was applied to the two sets of images D1 and D2 to get regions of interest (ROIs). This mask was projected into the right hemisphere and then is mirror-reflected using horizontal reflection of the left hemisphere. This process correlates the same regions in right and left hemispheres and allows to investigate bilateral symmetry. 528 regions of interest (264 for images for glioma and 264 for healthy patients) were obtained.

The following steps were performed:

(I) Two datasets are generated: D1 and D2,

(II) select ROIs for further image manipulation tasks; insert and crop out the rectangle ROIs to analyze the similarity for D1 and D2. It consisted of:

(a) design the first rectangle mask in the right hemisphere,

(b) determine the distances to generate the other two rectangle masks in the right hemisphere,

(c) insert the other two masks into the right hemisphere according to the distances from step (b),

(d) perform the mirror reflection of the masks into the right hemisphere onto the left hemisphere.

(III) crop out ROIs from both hemispheres, following the algorithm of step (II),

(IV) compute SSIM for monochrome ROIs,

(V) segment ROIs with the skeleton algorithm,

(VI) compute S-Jaccard for ROIs processed in step (V),

(VII) carry out a k − means clustering over SSIM and S-Jaccard values and pathologies,

(VIII) clusters analysis with silhouette method,

(IX) classification data using ROC analysis.

The region of interests cut from the right hemisphere were labelled as ROI 1R, ROI 2R, ROI 3R, and their symmetric in the left hemisphere were denoted as ROI 1L, ROI 2L, ROI 3L. Figure 3.2 shows examples for the implementation of SSIMs for right-left correspondents for a raw image containing Rician noise (left panel) and a filtered image by the anisotropic diffusion filter (right panel).

Figure 3.2 Example of cutting out ROIs in PD image for a patient with glioma. Left side: (a) raw image. Right side: (a) denoised image. (b) ROI 1L; (c) ROI 2L; (d) ROI 3L; (e) ROI 1R; (f) ROI 2R; (g) ROI 3R.

Figure 3.3 shows examples for the implementation of skeletonization for right-left correspondents for a raw image containing Rician noise (left panel) and a filtered image by the anisotropic diffusion filter (right panel). Figure 3.4 summarizes the skeletoniz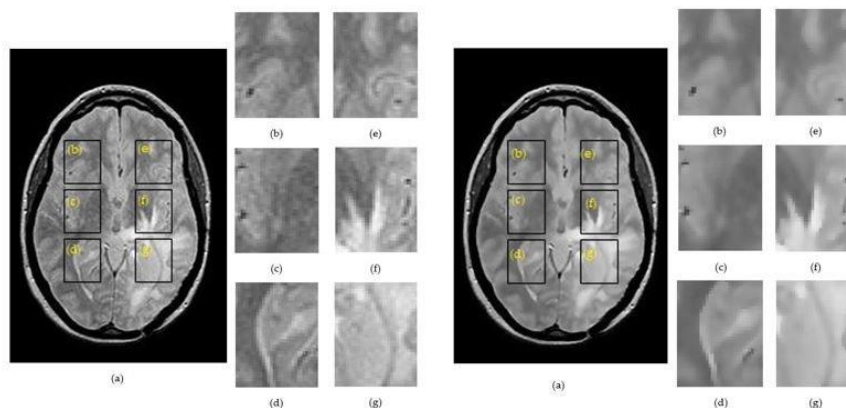ation results for a patient with glioma by providing a direct comparison of the morphological skeleton transform between brain hemispheres. The skeletal maps for two correlated ROIs were overlapped to provide a facile evaluation of dissimilarities.
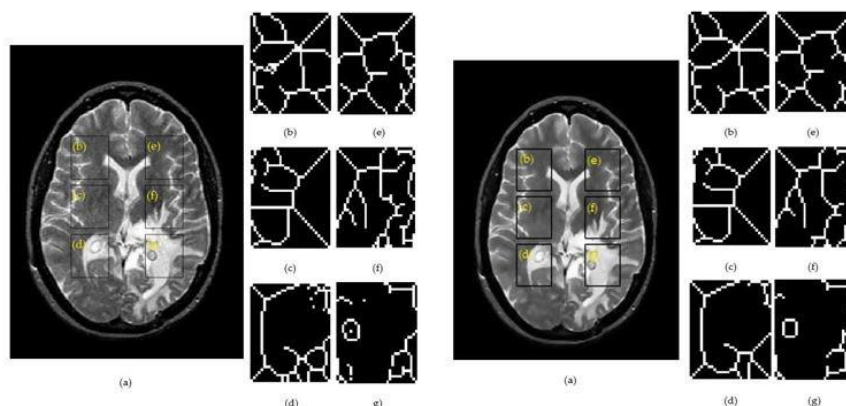
Figure 3.3 Results of the skeleton algorithm for a T2w image belonging to a patient with glioma. Left side: (a) raw image; Right side: (a) denoised image; (b) ROI 1L; (c) ROI 2L; (d) ROI 3L; (e) ROI 1R; (f) ROI 2R; (g) ROI 3R.
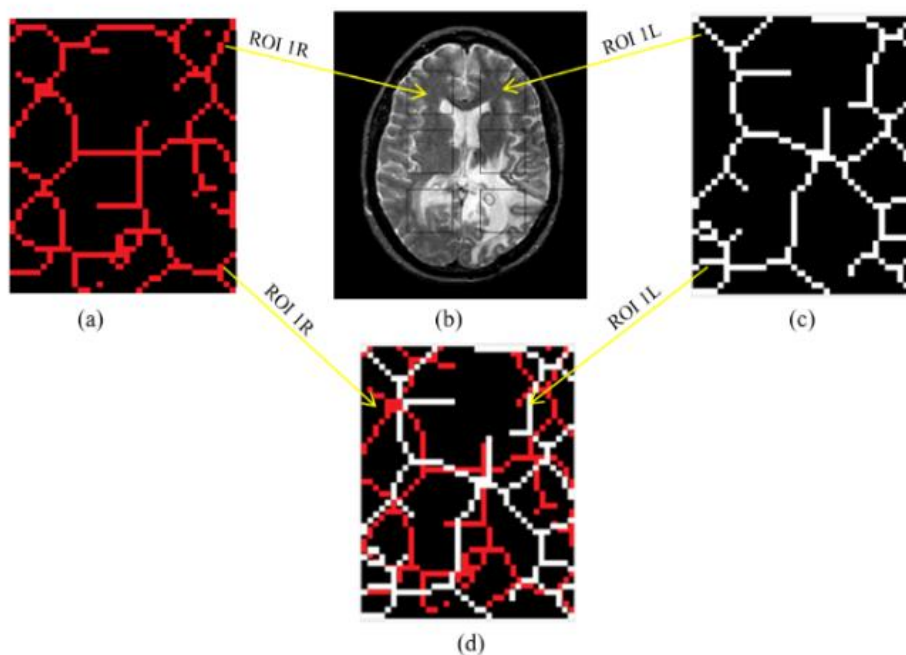
Figure 3.4 a) Skeletal map of ROI 1R; b) rectangular masks overlaid on a T2w MR image for a patient diagnosed with glioma; c) Skeletal map of ROI 1L; d) ROI 1R and ROI 1L overlapped to highlight differences between the skeletal maps.

K-mean clustering algorithm is used to group the n observations (i.e., SSIM and S-Jaccard values) into clusters. The number of clusters k = 3 follows the number of S-Jaccard 1 (between ROI 1R and its mirror symmetric ROI 1L), S-Jaccard 2 (between ROI 2R and its mirror symmetric ROI 2L) and S-Jaccard 3 (between ROI 3R and its mirror symmetry ROI 3L). The Silhouette method assesses the relative quality of the clusters and provides information on the data configuration and clustering validity. The results for S-Jaccard are shown in Figures 3.6 - 3.9, for ROIs PD and T2w MR images of set D1 (noisy images) and D2 (noisy images), respectively.

(**a**) SSIM_ healthy/T2w

(**b**) SSIM_ glioma/T2w

(**c**) SSIM_ healthy/PD

(**d**) SSIM_ glioma /PD

Figure 3.5 Cluster validity for SSIM values for raw images belonging to D1. The name of the images follows the pattern: Diagnose Index / MR image type

(**a**) SSIM_ healthy /T2w

(**b**) SSIM_ glioma/T2w

(**c**) SSIM_ healthy /PD

(**d**) SSIM_ glioma /PD

Figure 3.6 Cluster validity for SSIM values for denoised images belonging to D2. The name of the images follows the pattern: Diagnose Index / MR image type

Eng. Toporaș (Pană) Lenuța – *Applications of DWI and DTI scanning techniques for rapid assessment of specific parameter changes in brain disease*

Chapter 3 - Original contributions on identifying fundamental texture primitives for brain lesion differentiation

(**a**) S-Jaccard_ healthy/T2w

(**b**) S-Jaccard_ glioma/ T2w

(**c**) S-Jaccard_ healthy/PD

(**d**) S-Jaccard_ glioma/ PD

Figure 3.7 Cluster validity for S-Jaccard values for images belonging to D1. The name of the images follows the pattern: Diagnose Index / MR image type

(**a**) S-Jaccard_ healthy/T2w

(**b**) S-Jaccard_ glioma/T2w

(**c**) S-Jaccard_ healthy/PD

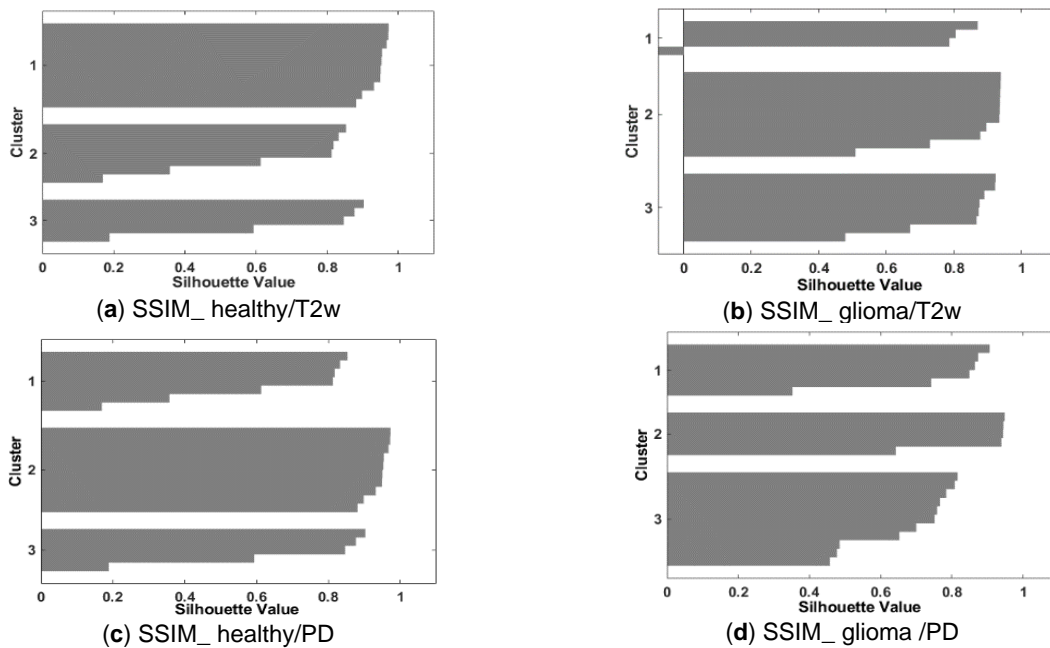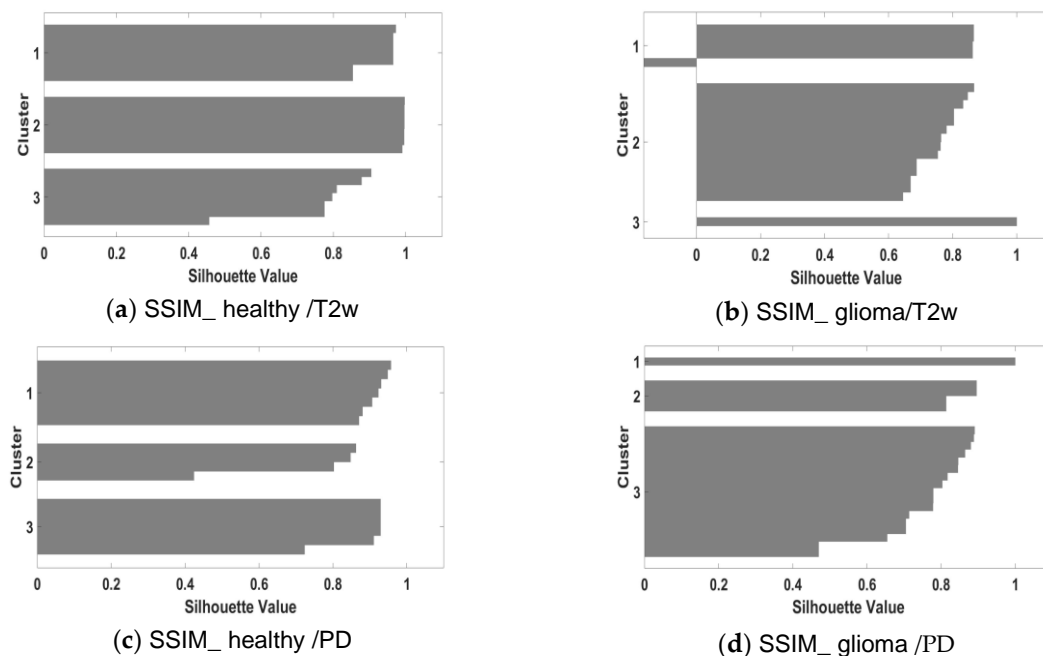(**d**) S-Jaccard_ glioma /PD

Figure 3.8 Cluster validity for S-Jaccard values for denoised images belonging to D2. The name of the images follows the pattern: Diagnose Index / MR image type
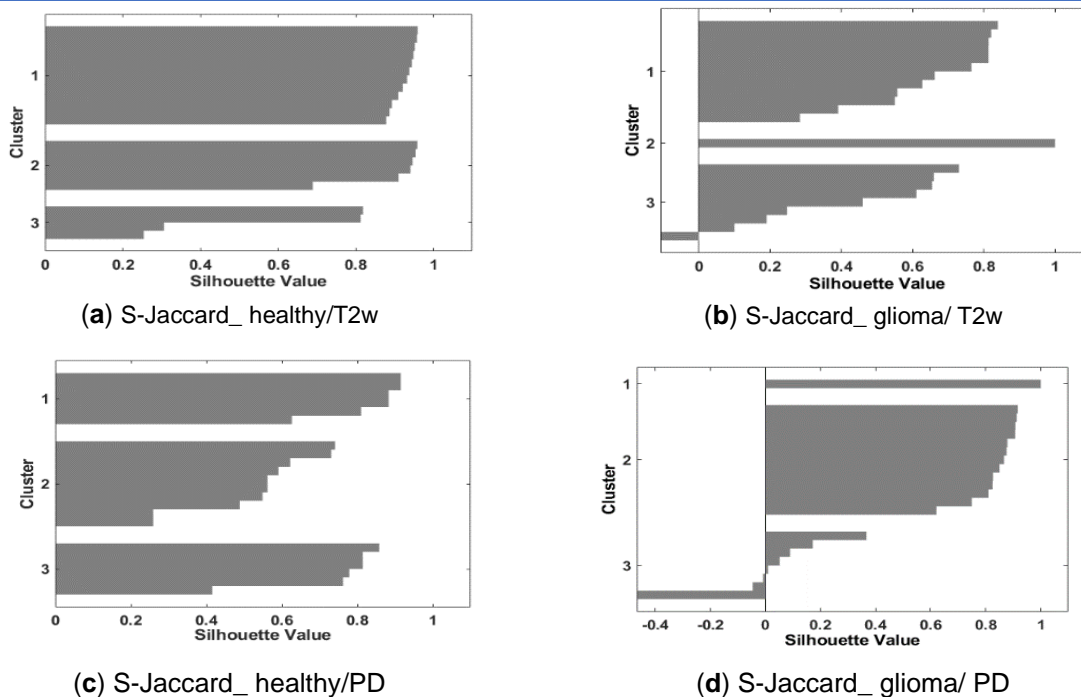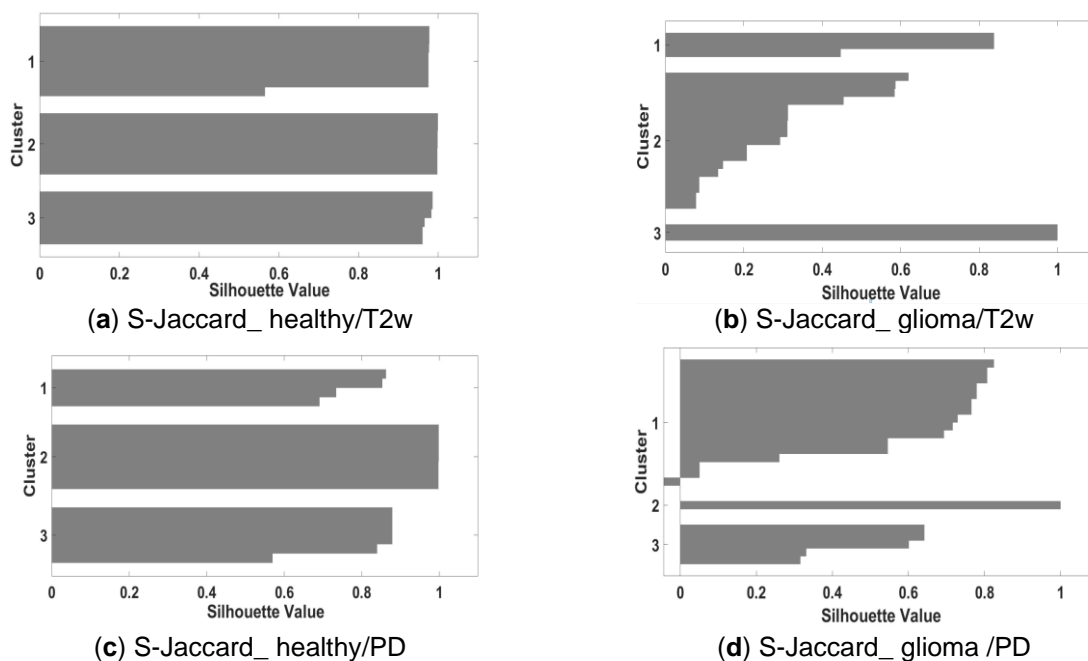
It can be noted the two cases of negative clusters (glioma/T2w, glioma/PD). Thus, for S-Jaccard_glioma / PD case $S(i) = -0.45$ for S-Jaccard_glioma / T2w case $S(i) = -0.1$, and SSIM_

Eng. Toporaș (Pană) Lenuța – *Applications of DWI and DTI scanning techniques for rapid assessment of specific parameter changes in brain disease*

Chapter 3 - Original contributions on identifying fundamental texture primitives for brain lesion differentiation

glioma/ T2w is characterized by S(i) = - 0.05 indicating an intermediate case lying far from the other two clusters or that analyzed objects are dispensed to another closest cluster. However, for denoised images these negative clusters are substantially reduced. Table 3.1 show that data indicated a clear cluster structure, exceptions for SSIM_glioma /PD and S-Jaccard_glioma/T2w to noisy images in D1. A better clustering performance is for database D2(when a denoising operation was carried out).

Table 3.1 The SC values for both pathologies and MR image type

Diagnosis / MR image type	SSIM (Dataset D1)	SSIM (Dataset D2)	S-Jaccard (Dataset D1)	S-Jaccard (Dataset D2)
Healthy /T2w	0.996	0.998	0.894	0.999
Glioma/T2w	0.998	0.998	**0.656**	0.999
Healthy /PD	0.953	0.961	0.881	0.998
Glioma/PD	**0.901**	0.921	0.980	0.991

The ROC curves plotted in figure 3.9 for raw and denoised images. The accuracy of the proposed skeletonization method is smaller for original images affected by Rician noise (AUC = 0.883 (T2w) and 0.904 (PD)) but increases for denoised images (AUC = 0.951 (T2w) and 0.969 (PD)).
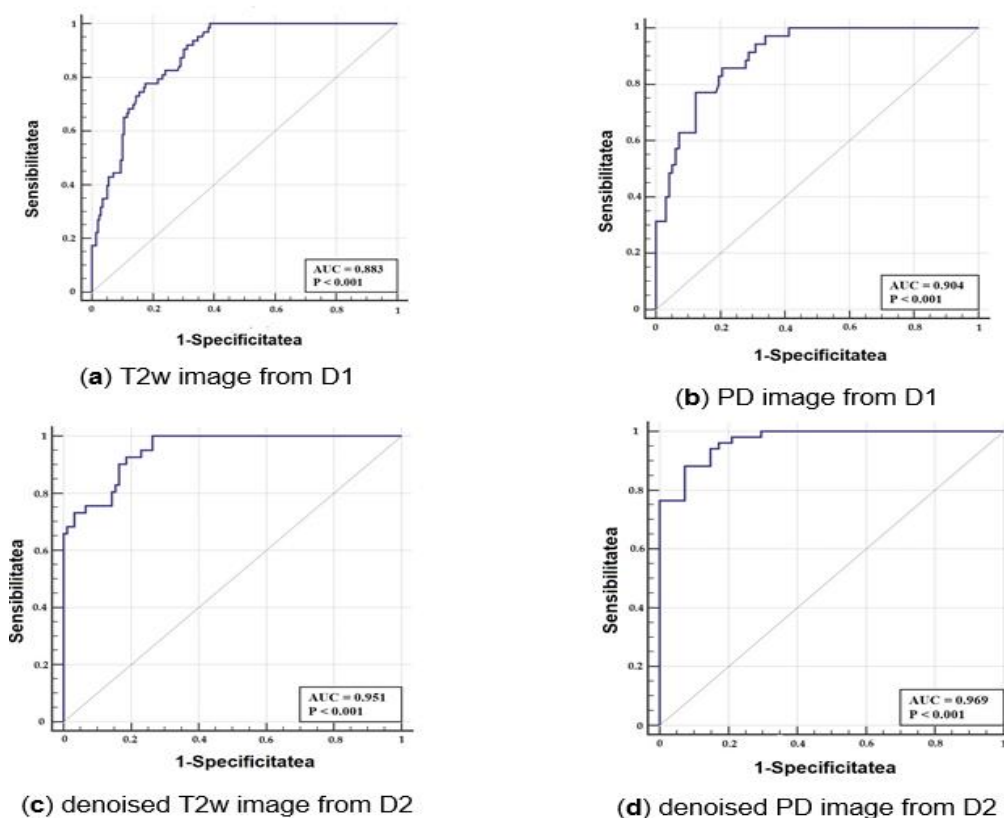

(a) T2w image from D1

(b) PD image from D1

(c) denoised T2w image from D2

(d) denoised PD image from D2

Figure 3.9 ROC curves for S-Jaccard computed for glioma images in D1 dataset (top) and D2 dataset (bottom).

Table 3.2 The cut-points ER and related sensitivity and specificity values, for S-Jaccard computed for glioma images

S-Jaccard	AUC	Sensitivity	Specificity	ER
denoised T2w image	0.951	0.927	0.813	0.2
denoised PD image	**0.969**	**0.882**	**0.926**	**0.139**
raw T2w image	0.833	1	0.657	0.343
raw PD image	0.904	0.857	0.794	0.25

The cut-points ER and related sensitivity and specificity values Table 3.2 shows. The case of glioma denoised PD images meet the condition that the sensitivity and specificity values are almost equal to AUC value. The average SNR is 18.5 dB for T2w images and 14.72 dB for PD images. As the SC, AUC and ER values for S-Jaccard index are higher for images in D2, we can conclude that edges are preserved and there were no artifacts generated during denoising operation. The skeletons generated from the tumoral areas and the reference healthy brain are compared using the scatter plots displaying the relationship between the length of each skeletal segment and the number of segments having the same length. The trend lines for each analyzed ROI were determine based on the length of each skeleton segment are presented in Figures 3.10 and 3.11. As can be seen polynomial trend curves allow an easier detection of the dissimilarity of skeleton maps. The length of each segment in skeleton map is determined using the Cartesian coordinates of the start and end points and the Euclidian distance. A scatter plot displaying the relationship between the length of each skeletal segment and the number of segments having the same length is built. The similarity of the polynomial curves is an indicator of the structural similarity between the healthy/reference and the source skeleton map and allow us to estimate the new edges generated due to the tumor presence empirically.
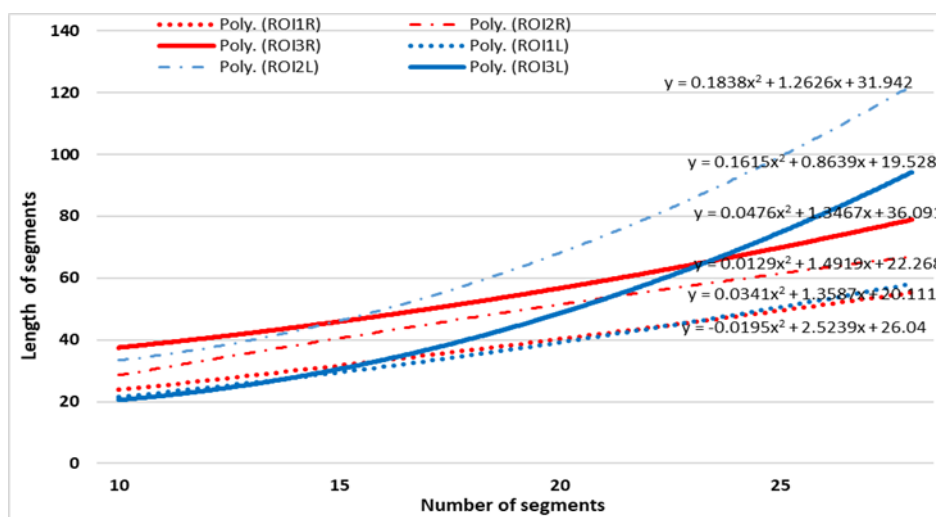
Figure 3.10 Fitted curves on number of skeleton segments vs. length of the segments (i.e., the corresponding connected pixels) for T2- weighted image for a patient with glioma
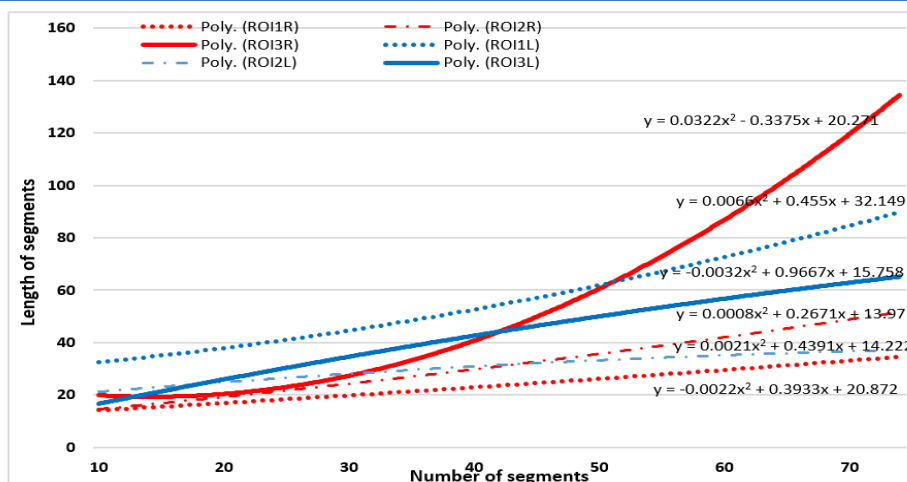
Figure 3.11 Fitted curves on number of skeleton segments vs. length of the segments (i.e., the corresponding connected pixels) for PD-weighted image for a patient with glioma

As a conclusion of this study a skeletal similarity empirical method using the comparison of the trend lines of skeleton maps datasets indicated PD- weighted image type as a better approach when the analysis is focused on edge detection, as it is suitable to very satisfactory edge-preserving results. At this stage of the study, S-Jaccard could be successfully used to differentiate healthy patients from those diagnosed with glioma.

The data from this study has been published in the article "*Brain tissue evaluation based on skeleton shape and similarity analysis between hemispheres*", **L. Pana**, S. Moldovanu, N. Dey, A. S Ashour și L. Moraru, Computation, Volume 8, 2020, Issue 2 [247].

Eng. Toporaș (Pană) Lenuța – *Applications of DWI and DTI scanning techniques for rapid assessment of specific parameter changes in brain disease*

Chapter 4 - Original contributions on 3D reconstruction and analysis of the brain

Chapter 4 - Original contributions on 3D reconstruction and analysis of the brain

4.2. 3D Enhancing spatial quality of MR images using statistical filters

This study aims to evaluate the efficacy of the spatial statistical filters like Maximum (Max) and Minimum (Min) filters for DTI images of a healthy patient and a patient diagnosed with ischemic stroke. A binarization operation has been applied to processed images and a similarity investigation was performed using the Dice score. A dataset of 2D processing images is used for the construction of the 3D images by means of the volume imaging technique using ImageJ. The effectiveness of the 3D construction imaging algorithm was investigated through the mean of the volume computation.

Two datasets for a healthy patient and a patient with ischemic stroke were investigated. This study includes 202 brain DTI images (128 × 128 pixels) in the DICOM format acquired without diffusion gradients ($b_0 = 0$ s/mm^2). The DTI images were acquired using a 1.5 T MRI scanner Philips Medical Systems, Best, Netherlands from "Sfântul Andrei" Hospital, Galați. The Research Ethics Committee of the "Dunărea de Jos", University of Galați, and "Sfântul Andrei" Hospital, Galati approve to use these images for research studies. Also, the informed consent was signed by every patient. The experiment is conducted following the steps in Figure 4.12:
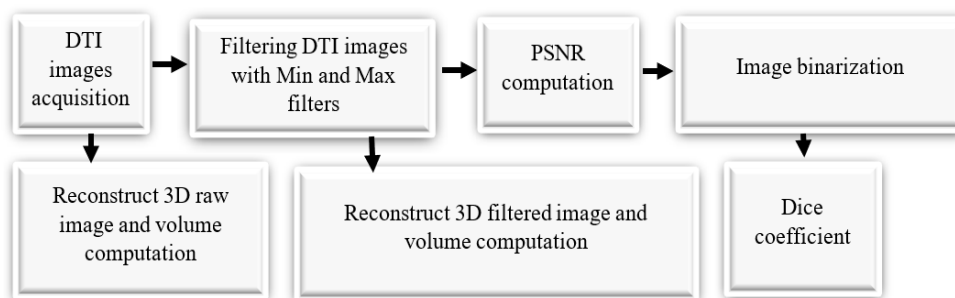
Figure 4.12 Flowchart of the proposed algorithm

Figure 4.13 displays the Dice score distribution for healthy and ischemic stroke patients and for Min and Max filtering operations. The Dice score has been computed between the original and the filtered images. Initially, the images were filtered and, subsequently, the filters' output were binarized using the Otsu thresholding algorithm. Results show that the Max filter yielded the best performance for both image datasets. However, there are no sharp differences between the Dice score values of the two filtering methods. The Dice values have an even distribution across images with a variation for first image in the stack. This variation is more pronounced for the ischemic stroke patient. Table 4.1 shows the mean   standard deviation values of the PSNR and Dice score for our method. Dice scores are higher for Max filter and for both patients. Thus, for healthy patient Dice score for Max filter is 3.63% higher than Min filter and 4.54% higher for diseased patient, respectively. In the case of PSNR, the Min filter is 2.12% higher for healthy patient and 3.30% higher for diseased patient.
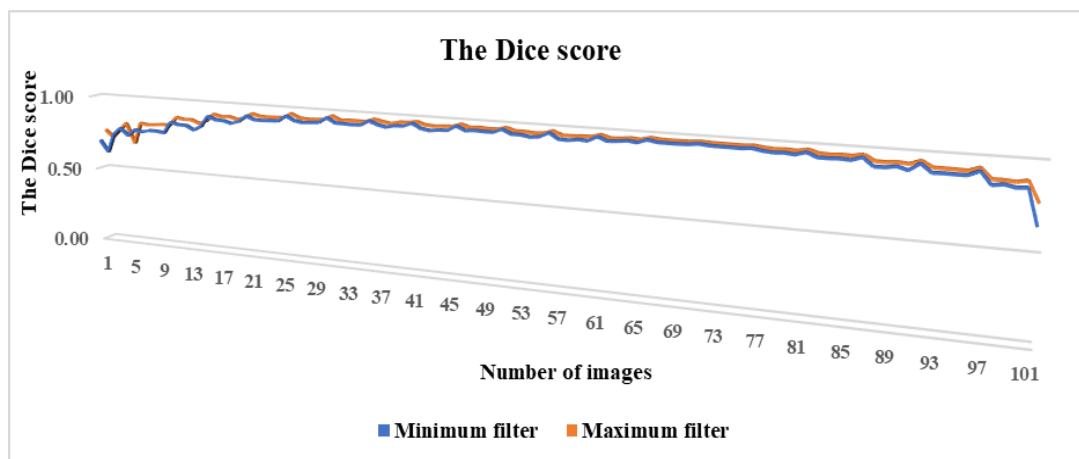
a)
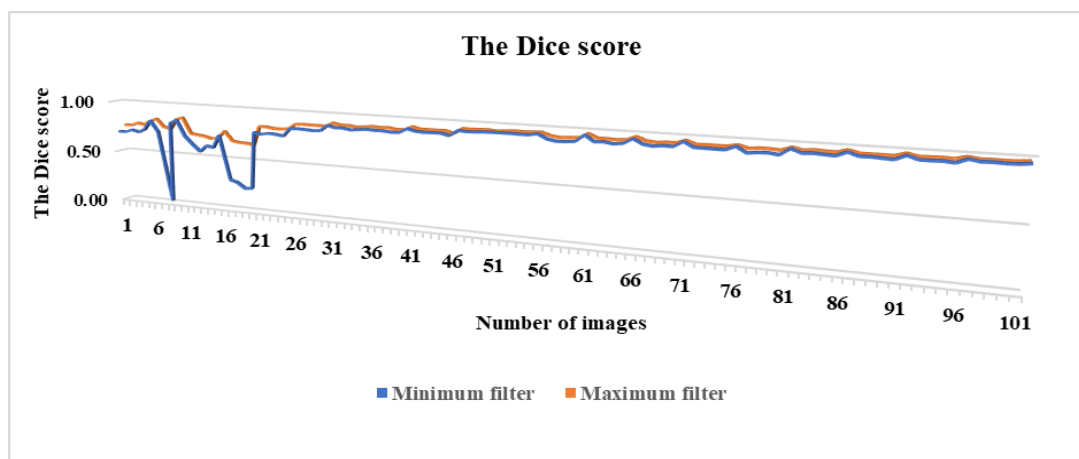
b)

Figure 4.13 Dice score for brain DTI images: (a) healthy patient; (b) ischemic stroke patient.

Tabel 4.5 The Mean (M) $\pm$ standard deviation (σ) values of the PSNR and Dice score for each filter and patient

Features	Maximum Filter (M $\pm$ σ)	Minimum Filter (M $\pm$ σ)
PSNR [dB]/healthy	21.5417 $\pm$ 2.1073	22.0093 $\pm$ 2.2899
PSNR [dB]/ ischemic stroke	22.2953 $\pm$ 3.1063	23.0562 $\pm$ 2.9938
Dice/ healthy	0.9247 $\pm$ 0.059	0.8911 $\pm$ 0.0693
Dice/ ischemic stroke	0.8888 $\pm$ 0.0851	0.8484 $\pm$ 0.1707

The noisy pixels appear as white (salt) and black (pepper) in images. The Min filter replaces the central pixel with the darkest one (i.e., removes the "salt") in the running window and the Max filter changes it with the lightest one (i.e., removes the "pepper"). A higher PSNR value in Table 4.5, indicates a better salt denoising. It is important to mention that binarization has been performed after filtering and that the Otsu method favors those pixels that have values above the set global threshold. In this case, the Maximum filter provides better results in terms of similarity

Eng. Toporaș (Pană) Lenuța – *Applications of DWI and DTI scanning techniques for rapid assessment of specific parameter changes in brain disease*

Chapter 4 - Original contributions on 3D reconstruction and analysis of the brain

with the original images. Overall, based on the noise removal performance and similarity of the data, we can conclude that Min filter is a better solution for filtering.

The volume of the 3D images has been used as a qualitative parameter to assess the feasibility of Min and Max filters in preprocessing medical data. In this case, 2D MR brain images are pre-processed before the construction of a 3D brain image using the proposed filters. Figures 4.14 and 4.15 show the results after the 3D construction of the 2D brain DTI images for an ischemic stroke and a healthy patient.

a)   b)   c)
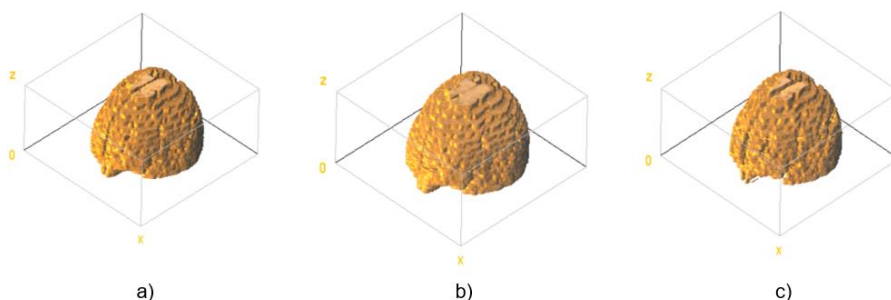
Figure 4.14 3D brain image for an ischemic stroke patient. (a) 3D image for the raw data; (b) 3D image for the Maximum filter; (c) 3D image for the Minimum filter. Both filters used a circular sliding window of 2 px size.

a)   b)   c)
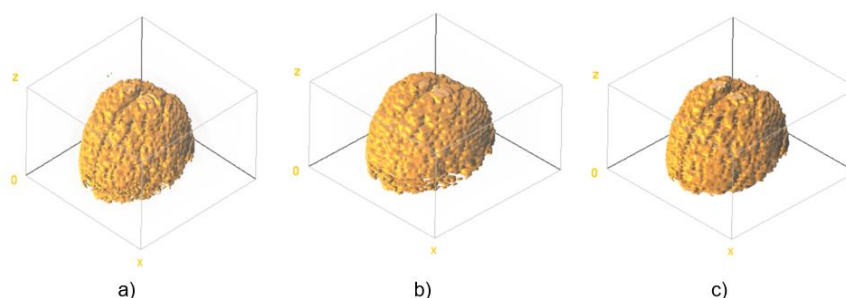
Figure 4.15 3D brain image for a healthy patient. (a) 3D image for the raw data; (b) 3D image for the Maximum filter; (c) 3D image for the Minimum filter. Both filters used a circular sliding window of 2 px size.

Tabel 4.6 Relevant the brain volume values for the proposed experimental conditions

Experimental conditions	V (10^6 pixels)	ΔV(%)
Volume/healthy/ raw images	2.41	-
Volume/healthy/ Maximum Filter	2.74	- 13.69
Volume/healthy/ Minimum Filter	2.29	+ 4.97
Volume/ ischemic stroke / raw images	2.28	-
Volume/ ischemic stroke / Maximum Filter	2.56	- 12.28
Volume/ ischemic stroke / Minimum Filter	2.15	+ 5.70

Table 4.6 contains the brain volume values for raw brain images and filtered images, for both patients. The volume variation is small and positive for Max filter and is larger and negative for Min filter, respectively. The Max filter enhances white pixel values in the image and increases the white area. On the contrary, the Min filter acts on the dark values in the image by increasing

Eng. Toporaș (Pană) Lenuța – *Applications of DWI and DTI scanning techniques for rapid assessment of specific parameter changes in brain disease*

Chapter 4 - Original contributions on 3D reconstruction and analysis of the brain

the dark area. It highlights the "pepper" type pixels and the number of "pepper" pixels in MR images belonging to the patient with ischemic stroke is higher. As a result, in this pathology the Min filter is a better solution for 3D reconstruction and volumetric analysis.

The data from this study has been published in the article „*Statistical Filters for Processing and Reconstruction of 3D Brain MRI*", **L. Pana**, S. Moldovanu, L. Moraru, 25th International Conference on System Theory, Control and Computing (ICSTCC), Iași, Romania, 2021, Pages 655-658 [256].

4.4. Local Graph Cut (LGC) and Flood Fill (FF) segmentation algorithms for multimodal MR images

This research aims to perform a comparative study on the performance of segmentation algorithms (LGC and FF) and 3D brain tumor volume reconstruction using 2D segmented regions of interest and obtain of MR brain image stacks. We tested our methods on multimodal image sets containing high graded glioma. The images were provided by the BraTS2020 dataset from the CBICA site [258, 259]. These multimodal scans are NIfTI files (.nii.gz or neuroimaging informatics technology initiative format) and are native (T1), T2-weighted (T2) and T1ce contrast-enhanced. Also, the BraTS2020 provides the ground truth (GT) images that are the same imaging datasets manually segmented by experienced neuro-radiologists. For our study we have used 469 T1, 469 T1ce, T2w and 469 GT images. Figure 4.19 shows some examples of used images.
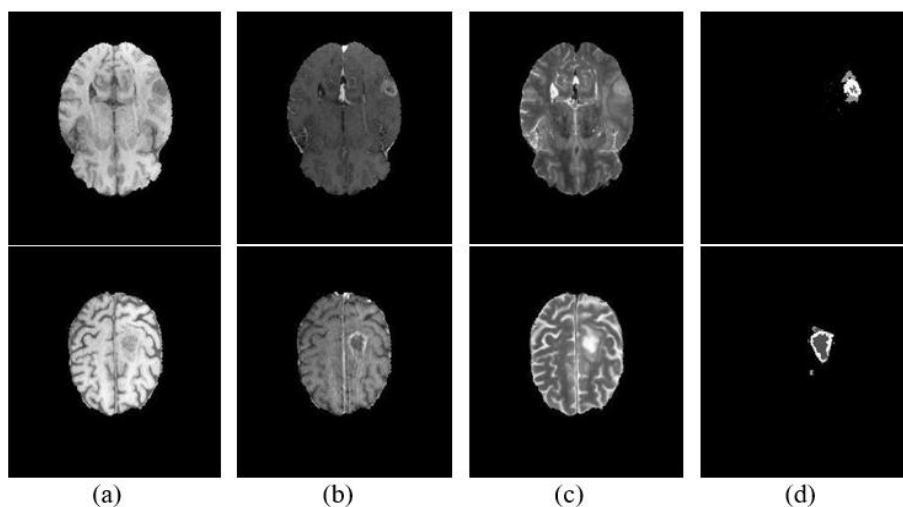
Figure 4.19 Examples of glioma images from BraTS2020.
(a) tumor visible in T1 MR brain image; (b) tumor visible in T1ce MR brain image; (c) tumor visible in T2w MR brain image; (d) the ground truth GT segmentation,

The study steps are presented in Figure 4.20 and they include:
→ acquisition of the images,
→ sequential application of the LCG and FF segmentation methods on each MR images type,
→ computed the Dice coefficient scores for the brain tumors segmentation in relation to the ground truth tumors provided by the BraTS2022 database,
→ 3D tumor brain image reconstruction and volume computation.

Eng. Toporaș (Pană) Lenuța – *Applications of DWI and DTI scanning techniques for rapid assessment of specific parameter changes in brain disease*

Chapter 4 - Original contributions on 3D reconstruction and analysis of the brain
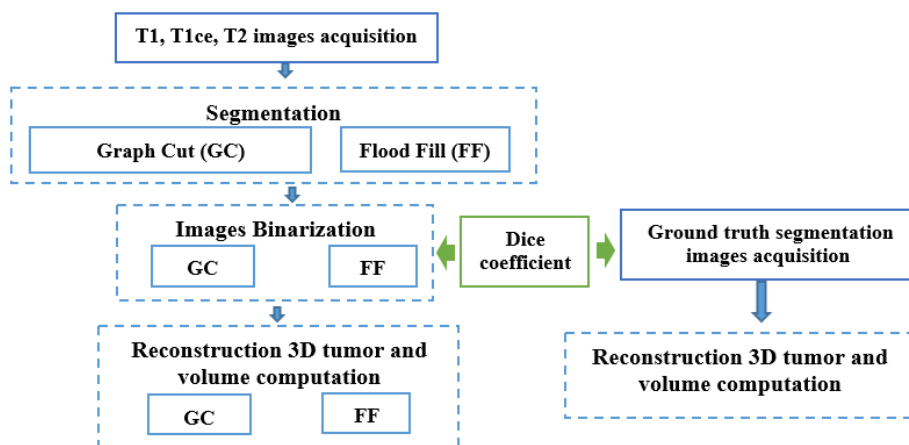
Figure 4.20 Overview of the proposed method

Figure 4.21 shows both tumor localization and segmentation results of LGC and FF segmentation algorithms, on certain selected samples.
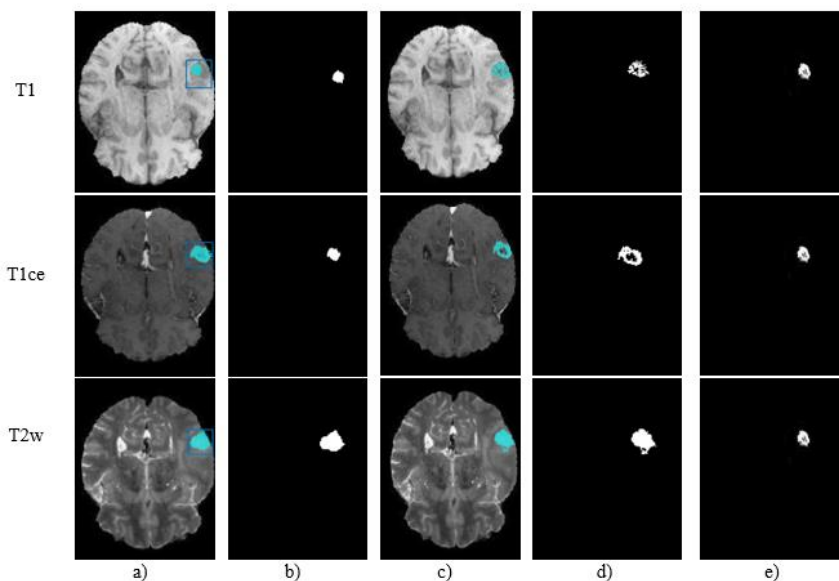
Figure 4.21 Examples of the segmentation results with the proposed methods. Each row presents an MRI scan modality. (a) raw MR image from BraTS2020 with the tracking window designated by users in the framework of LGC algorithm; (b) LGC tumor segmentation result; (c) raw MRI from BraTS2020 with the marked portion in image. To run the FF algorithm, we have located the seed point in the upper left corner of the image; (d) FF tumor segmentation result; (e) glioma tumor ground truth

To evaluate the brain tumor segmentation, the Dice coefficient is computed. It is an agreement score between the segmentation results in LCG-GT and FF-GT pairs and serves as a quality metric. Table 4.9 tabulates the Dice score for both segmentation methods.

Eng. Toporaș (Pană) Lenuța – *Applications of DWI and DTI scanning techniques for rapid assessment of specific parameter changes in brain disease*

Chapter 4 - Original contributions on 3D reconstruction and analysis of the brain

Table 4.9 Dice coeficient comparison (Mean M± standard deviation σ) between segmentation methods

Segmentation method	Types of images	Dice score (M ± σ)
LGC-GT	T1	0.226 ± 0.107
	T1ce	0.323 ± 0.125
	T2w	**0.501 ± 0.128**
FF-GT	T1	0.236 ± 0.131
	T1ce	0.338 ± 0.111
	T2w	0.483 ± 0.155

The best results are obtained for T2-w images and LGC algorithm corresponding to value of 0.501 0.128. We can observe that there are not important differences between the results provided by investigated algorithms for all images types. As can be seen that the performance of used methods is relatively poor. The main reason is the suboptimal neuroimaging quality due to clinical circumstances. Also, we have tested a variety of MRI imaging modalities and the used algorithms have pros and cons related to the effectiveness of their implementation. The segmentation results are not as accurate as expected but the methods we tested provide the most reliable segmentations under the circumstances that the MRI quality is limited.
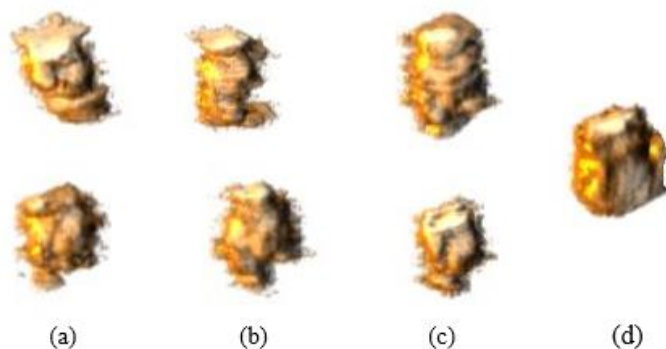
Figure 4.22 3D visualization results of the proposed methods. First row is for LGC algorithm and the second row is for FF algorithm, respectively. (a) T1 MRI scan modality; (b) T1ce MRI scan modality; (c) T2 MRI scan modality; (d) ground truth.

Further, the segmented 2D tumor brain images are converted into 3D surface models using the ImageJ plugin. Figure 4.22 shows 3D reconstruction results of brain tumors segmented by proposed methods and for each MR image type, belonging to the same patient. With Volume Viewer command, for each analyzed case, 45 slices were used with the interval of 1.5 pixels or 0.3967 mm, for rendering 3D tricubic smooth interpolation volume in xyz space. The obtained result shows that 3D visualization maps clearly represent the size and shape of the segmented tumor so that the volume of the tumor could be estimated. Also, the orientation of the 3D objects can be freely adjusted.

Table 4.10 contains the brain volume values for segmented images. As a result, the LGC is a better solution for 3D reconstruction and volumetric analysis by using T2 image type.

Table 4.10 The tumor brain volume values

Segmentation method	Image type	Volume $\times 10^6$ (voxel)
LGC	T1	1.145
	T1ce	1.213
	T2w	**1.619**
FF	T1	1.313
	T1ce	0.863
	T2w	**1.449**
GT		**2.255**

These average data on the tumor volume values allows us to assess how the tumor's anatomy, in the generated images, match the real ones provided by the ground truth images. An average, a 71,8% match is obtained. This variation in the results could be attributed to the low accuracy in terms of contrast between tissue and to certain geometric distortions inherent to MRI technique. However, the tumor's anatomy in the generated images match real ones provided by the ground truth images.

The data from this study has been published in the article „*3D Brain Tumor Volume Reconstruction and Quantification using MRI Multi-modalities Brain Images*", **L. Pana**, S. Moldovanu, L. Moraru, The 10th IEEE International Conference on E-Health and Bioengineering - EHB 2022, Grigore T. Popa University of Medicine and Pharmacy, Iași, Romania, 2022 [260].

Chapter 5 - Original contributions on utilizing Mutual Information from DTI images for image registration

5.1. Mutual Information from image registration criterion

In this chapter we present a rigid, multi-modal image registration algorithm based on linear transformation and oriented gradients for the alignment of T2-weighted (T2w) images (as a fixed reference) and diffusion tensor imaging (DTI) (b-values of 500 and 1250 s/mm^2) as floating images of three patients. The declared goal is to compensate for the motion during the acquisition process. Three datasets were investigated. They were denoted as S1 for a healthy patient (36-year-old male), S2 for a patient (68-year-old male) with right parietal lobe hemorrhage and a small sequela in the right hemisphere, and S3 for a patient with ischemic stroke (74-year-old male). Each dataset includes three T2w images with15 slices per image, three DTI (b-values = 500 s/mm^2) images with 15 slices per image, and three DTI (b-values = 1250 s/mm^2) images with 15 slices per image. The procedure was applied to pairs of T2w-DTI (b-values = 500 s/mm^2) and T2w-DTI (b-values = 1250 s/mm^2). DTI sequences were acquired using a system with six-channel sensitivity encoding (SENSE) for faster scanning (FS = 1.5). The imaging parameters were as follows: 3D gradient echo with echo time (TE) ranging from 83 to 110 ms; repetition time (TR) ranging from 6500 to 7800 ms; bandwidth = 1070 Hz/pixel; flip angles (2^0 and 6^0); voxel resolution ranging from 2.5 to 3.0 mm; and slice thickness = 4 mm. The acquisition matrix was 128 × 128. A T2w scan was performed without coil using identical parameters. The images were skull stripped and no other preprocessing was applied. Approval for the study was obtained from the Research Ethics Committee of the "Dunarea de Jos" University of Galati, and "Sfântul Andrei" Hospital. The patients' informed consent was obtained in writing from each patient involved.

To overcome the limitations of multi-modal medical image recordings, a new solution criterion is proposed by using the Mutual Information (MI) method or mutual information using the histogram of oriented gradients (HOG, Histogram of Oriented Gradients) of the image.

The proposed method relies on the whole brain surface and addresses the variability of anatomical features into an image stack. The sparse features namely, the spatial information of pixels refer to corners detected using the Harris corner detector operator, while dense features, those high gradient values around edges and corners, are detected using the HOG histogram. The histograms of oriented gradients are used to compute entropy of the source and target images, as well as the joint entropy of both images.

The optimal translation parameter т was identified by using the method of the smallest values of the Euclidean distance (ED) to eliminate significant scale differences. Fine registration is given by the rotation parameters of the rigid transform Θ followed by HOG feature extraction and MI computation to find the best matches between registered images.

The accuracy of the registration and the quantification of the registration error is performed by the fiducial registration error (FRE) driven by the minimization of the distance between the selected Harris corners in both images after registration. A low FRE value signifies good registration accuracy. The selected fiducial points (|Ω|) are spread evenly over the whole brain image and represent the Harris corners. We used |Ω| = 30 corner points for the T2w and DTI (b-values of 500 and 1250 s/mm^2) images. |Ω| represents the minimum number of corresponding corners identified in all analyzed images and they have the smallest possible distance, according to the ED values.

Also, the root mean square (RMS), mean and standard deviation of the FRE values were determined, after the image registration is performed.

Our method improved registration efficiency, robustness, and reduced computational cost compared with other registration algorithms, which use anatomical features or regions of interest areas with specific neuroanatomy. The relative start and end positions of the image stacks provide the pre-requisites for a diversity of spatial and intensity information, leading to robust registration.
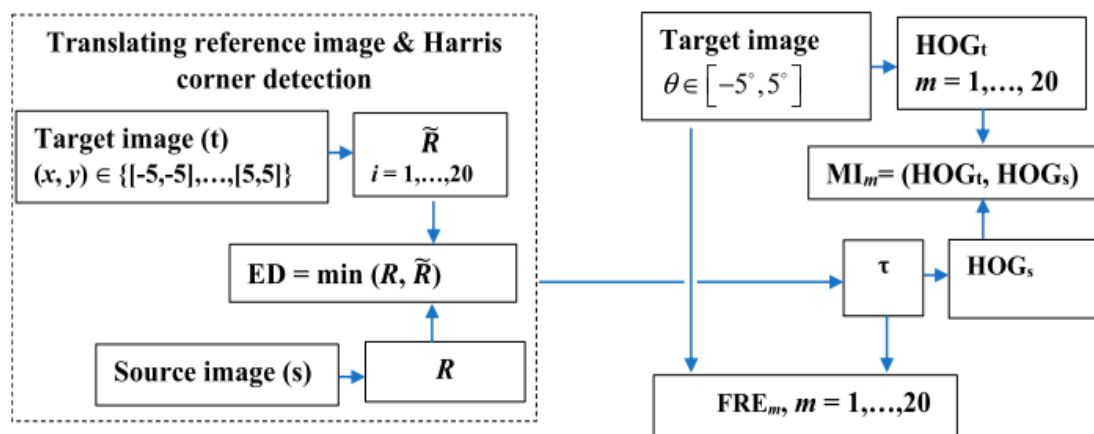

Figure 5.1 A flowchart. In the left block, the coarse registration step is displayed. The translation vector over the x and y axis; R and e R corner points in the source (s) and target/registered (t) images, respectively; and the Euclidian distance (ED) between similar strong corners are determined. i = 1,...,20 is the incremental step for translational operation with a step of 0.5. In the right block, the fine registration based on the rotation is performed and histograms of gradients (HOGs, HOGt) for the source (s) and target (t) images are determined. Then, mutual information (MI) and fiducial registration error (FRE) are computed. m = 1,...,20 denotes the rotation operations with a step of 0.5.

The figure 5.1 shows a flowchart of the proposed registration method. The Harris operator was used to extract corner and edge information by setting k = 0.05 and T = 1500. These parameters were set empirically to ensure the best registration performance. Two translations in horizontal (x) and vertical (y) directions, were performed. The strong corners are robust to global changes of intensity. They are selected in the source (R) and the registered images ($\tilde{R}$) and the ED between similar strong corners in each pair of images were computed. The best new position after the translation process is determined using the smallest ED values.

After determining that two images have been correctly matched by an optimal value of the translation parameter τ, a rotation in the range θ ϵ [-5^0, +5^0] with a step of variation 0.5 is performed and histograms of the image gradients are generated, using the HOG algorithm.

We denoted by HOGs and HOGt the gradient histograms for the source (s) and the target (t) images, respectively. The fine registration stage amends and improves the misalignment and refines the registration performance through a local approach by HOG. Then, MI and FRE are computed. The experiment results for the translation of the registered images are provided in Figures 5.2 și 5.3. In the coarse registration step, the average number of sparse features/corners, per image, varied as follows:

- for S1, from 40 to 181 for T2w-DTI (b = 500 s/mm^2) and from 40 to 166 for T2w-DTI (b = 1250 s/mm^2),
- for S2, from 38 to 167 for T2w-DTI (b = 500 s/mm^2) and from 35 to 152 for T2w-DTI (b = 1250 s/mm^2),
- For S3, from 42 to 160 for T2w-DTI (b = 500 s/mm^2) and from 39 to 144 for T2w-DTI (b = 1250 s/mm^2)

The Harris corners are evenly distributed over the cerebral surface and are located in that spots where a large variation in intensity in all the directions manifests. These corners have similar locations and belong to the same regions, in the paired images. The locations of these corners show some variability, the mobility of the corners being however limited to a narrow range by the anatomical structure of the brain. In our case, the low corner mobility allows identifying and establishing the importance of Harris corners and helps generate paired Harris corners.

The optimal translation parameters are $\tau = \begin{pmatrix} \tau_x \\ \tau_y \end{pmatrix} = \begin{pmatrix} -4.5 \\ -4.5 \end{pmatrix}$ for S1, for S2 $\tau = \begin{pmatrix} \tau_x \\ \tau_y \end{pmatrix} = \begin{pmatrix} -2.5 \\ -2.5 \end{pmatrix}$ and for S3 $\tau = \begin{pmatrix} \tau_x \\ \tau_y \end{pmatrix} = \begin{pmatrix} 2.5 \\ 2.5 \end{pmatrix}$. They were identified using the smallest values of the ED values between corners strongly similar in position. These parameters ensure a coarse registration that allows the elimination of differences on a significant scale. This coarse registration step shortens the exploration range in the transformation model.

(b)   (c)

(a)   (d)   (e)

Figure 5. 2 Examples of pairwise linear registration/translation between source and target images, for a healthy patient, using corner points detection. Image labeling using the Harris operator. Detected corners have similar locations and belong to the same regions, but show certain mobility. The optimal translation parameter for a coarse registration is identified as τ = (−4.5; −4.5). The fixed/source image is displayed in green and the moving/target image in magenta. (a) T2w.(b) DTI (b = 500 s/mm^2). (c) T2w-DTI (b = 500 s/mm^2). (d) DTI (b = 1250 s/mm^2). (e) T2w-DTI (b = 1250 s/mm^2).

Eng. Toporaș (Pană) Lenuța – *Applications of DWI and DTI scanning techniques for rapid assessment of specific parameter changes in brain disease*

Chapter 5 - Original contributions on utilizing Mutual Information from DTI images for image registration

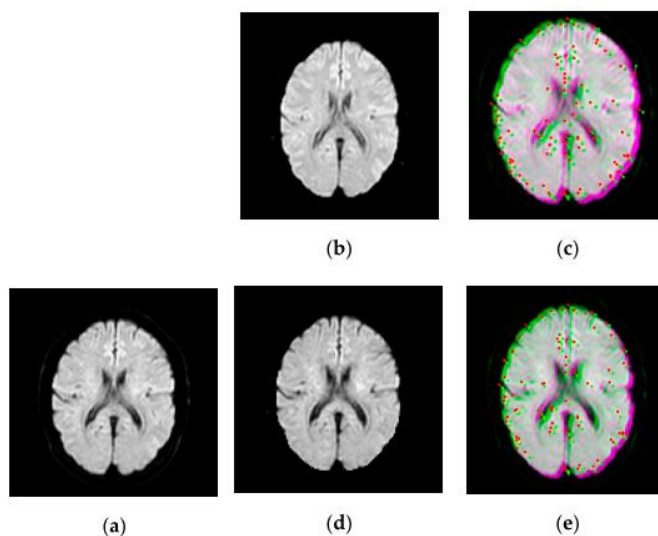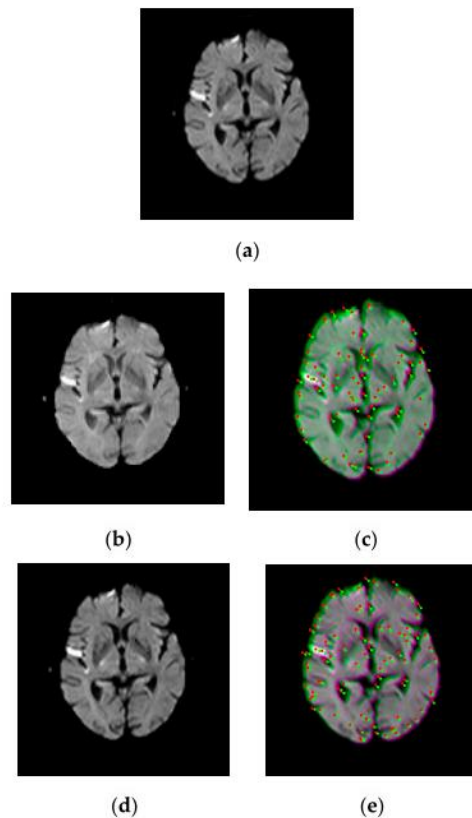*Figure 5.3 Examples of pairwise linear registration/translation between source and target images, for a patient with right parietal lobe hemorrhage, using corner points detection. Image labeling using the Harris operator. Detected corners have similar locations and belong to the same regions, but show certain mobility. The optimal translation parameter for a coarse registration is identified as τ = (−2.5; −2.5). The fixed/source image is displayed in green and the moving/target image in magenta. (a) T2w. (b) DTI (b = 500 s/mm^2). (c) T2w-DTI (b = 500 s/mm^2). (d) DTI (b = 1250 s/mm^2). (e) T2w-DTI (b = 1250 s/mm^2).*

For each completed rigid transformation image, the HOG algorithm is applied and the gradients and orientations of the edges, for all locations, are collected to generate the feature vectors and construct the HOG histograms. Figures 5.4 and 5.5 show examples of HOG features for subjects S1 and S2. Images are divided into areas/blocks of size 8 × 8 pixels. Then, the gradients for every pixel in the x and y directions are computed. The magnitude and direction for each pixel value are determined. To minimize the influence of lighting effects, the gradients were normalized by considering 16 × 16 blocks. Then, four 8 x 8 patches are combined to create a 16 x 16 block used to extract the HOG features. An 8 × 8 block contains abundant information, with the number of HOG features being 34.596.
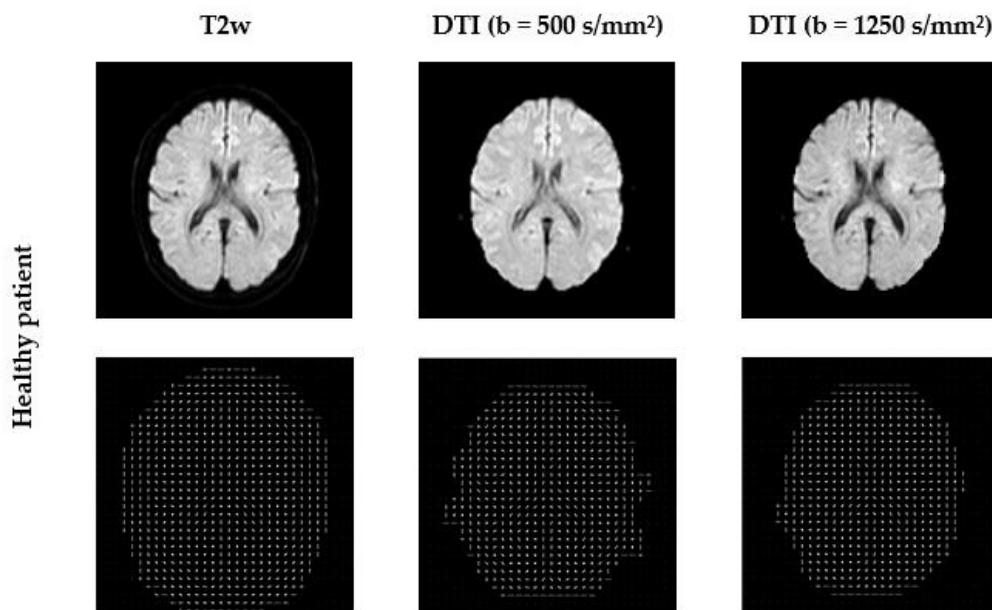
Figure 5.4 Examples of HOG features extracted from the original images for subjects S1. HOG computes block-wise histogram gradients with multiple orientations. An image is divided in 8 x 8 patches. A normalization of the gradients is performed by combining four 8 x 8 patches to create a 16 × 16 block for features extraction. A features vector has been computed and 34.596 features are extracted.
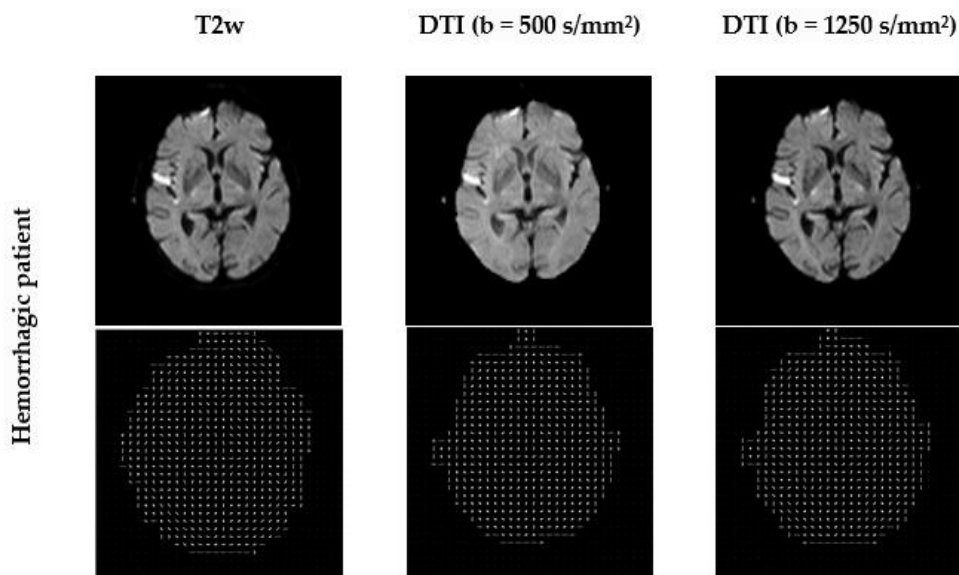
Figure 5.5 Examples of HOG features extracted from the original images for subject S2. HOG computes block-wise histogram gradients with multiple orientations. An image is divided in 8 x 8 patches. A normalization of the gradients is performed by combining four 8 x 8 patches to create a 16 × 16 block for features extraction. A features vector has been computed and 34.596 features are extracted

The MI is computed as a statistical intensity relationship between the corresponding pixels in both the source and target images. MI is accepted as the reference (gold standard) similarity

Eng. Toporaș (Pană) Lenuța – *Applications of DWI and DTI scanning techniques for rapid assessment of specific parameter changes in brain disease*

Chapter 5 - Original contributions on utilizing Mutual Information from DTI images for image registration

measure for multimodal image registration. However, there are no reference records (gold standard) available for T2w-DTI images registration-based HOG. So, the results of the proposed method are compared to the MI based on the image intensities of corresponding pixels (figure 5.6 and 5.7). Figure 5.6 shows examples for MI computed based HOG. The maximum MI values is obtained for the rotation and translation parameters as follows: for S1 (-2^0, -4.5 mm, -4.5 mm), for S2 (2^0, -2 mm, -2 mm) and for S3 (2.5^0, 2.5 mm, 2.5 mm), respectively.



(a)   (b)

(c)   (d)
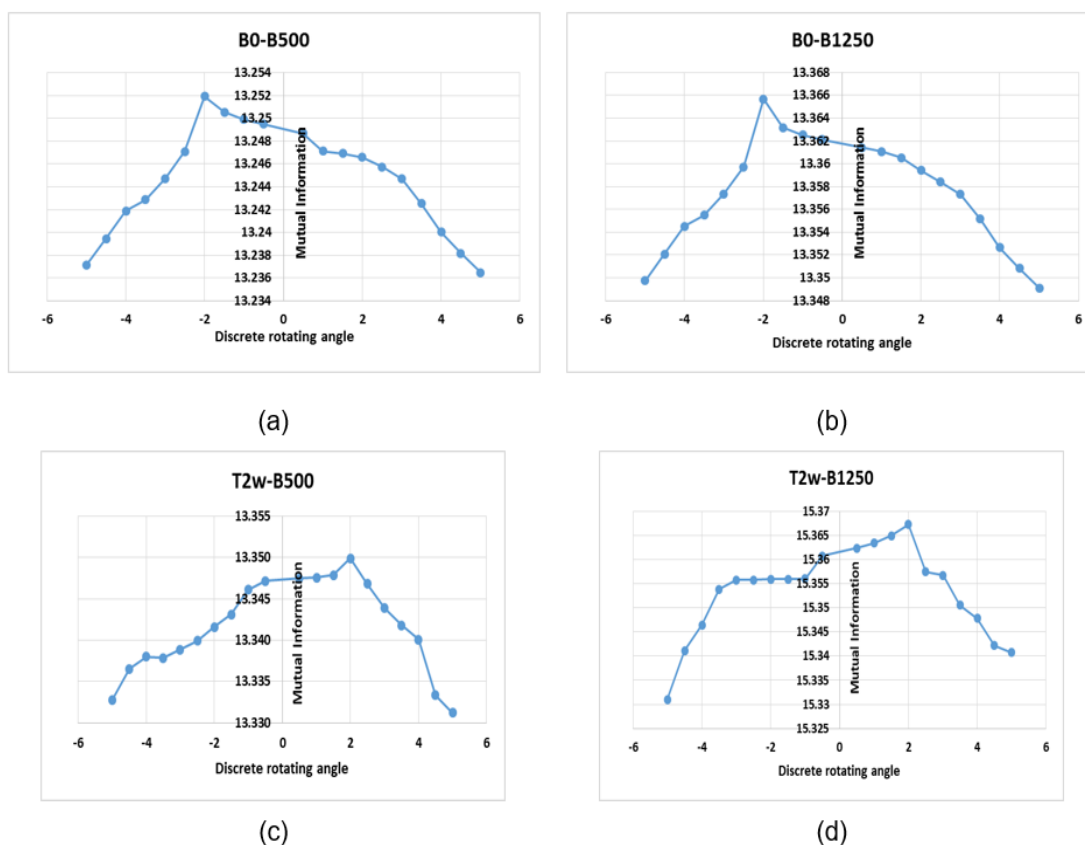
Figure 5.6. First row: MI based on histogram of gradients pattern for the healthy subject (S1), which depends on a rotation parameter in the range $\theta \in [-5^0, +5^0]$ with a step of variation of 0.5^0 and for a translational parameter of -4.5 pixels along the x and y axis. (a) T2w-DTI (b-values = 500 s/mm2) registration; (b) T2w-DTI (b-values = 1250 s/mm2) registration. These curves show a maximum at the correct points of alignment, i.e., (-2^0; 13.2507) for the left plot and (-2^0;13.3658) for the right plot. Second row: MI based on histogram of gradients pattern for the diseased subject S2, which also depends on a rotation parameter in the range $\theta \in [-5^0, +5^0]$ with a step of variation of 0.5^0 and for a translational parameter of -2.5 pixel along the x and y axis. (c) T2-w-DTI (b-values = 500 s/mm^2) registration; (d) T2-w-DTI (b-values = 1250 s/mm^0) registration. These curves show a maximum at the correct points of alignment, i.e., (2^0; 13.3501) for the left plot and (2^0; 15.3682) for the right plot.

Figure 5.7 shows examples of the MI variation computed using the statistical intensity relationships between the corresponding pixels in both the source and target images.

(a)

(b)

(c)

(d)

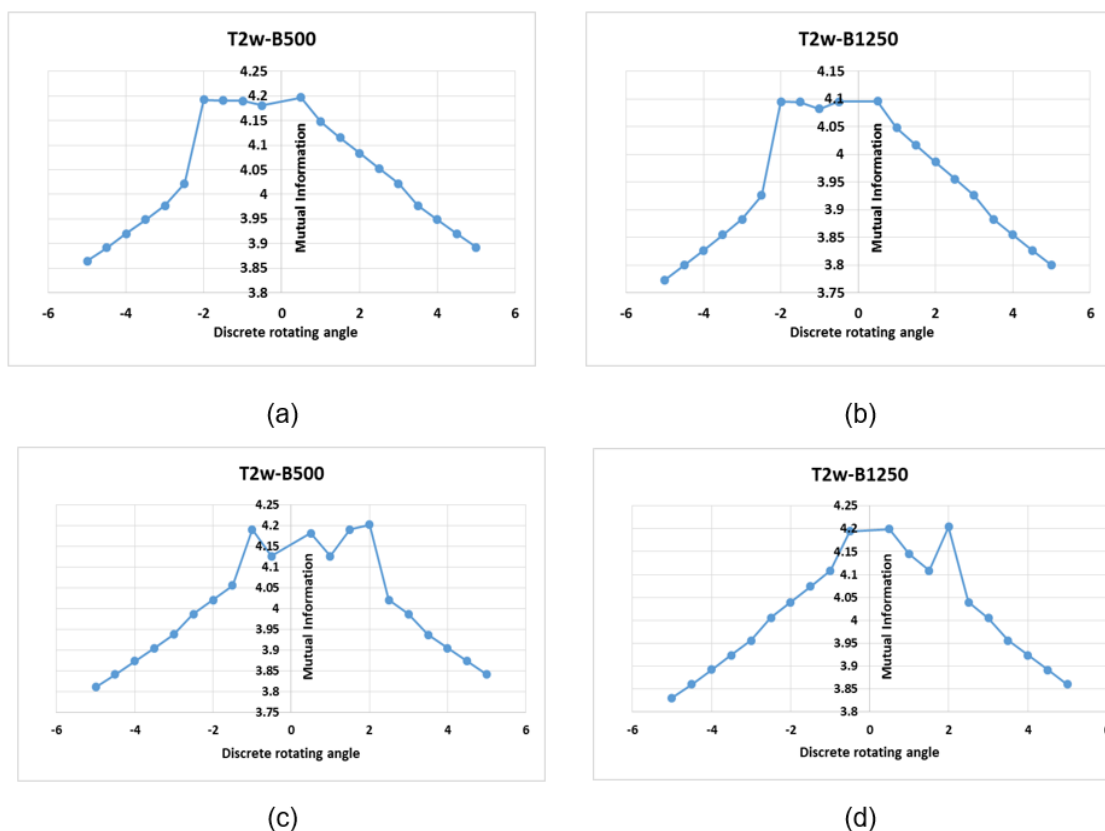*Figure 5.6 First row: MI pattern (as a statistical intensity relationship between corresponding pixels in source and target images) for the healthy subject S1, which depends on a rotation parameter in the range θ ∈[−5⁰, +5⁰] with a step of variation of 0.5⁰and for a translational parameter of −4.5 pixels along the x and y axis. (a) T2w-DTI (b-values = 500 s/mm²) registration; (b) T2w-DTI (b-values = 1250 s/mm²) registration. These curves show two local maxima, i.e., (−2⁰; 4.781) and (+0.5⁰; 4.948) for the left plot, and (−2⁰; 4.734) and (+0.5⁰; 4.901) for the right plot. Second row: MI pattern (as a statistical intensity relationship between corresponding pixels in source and target images) for the diseased subject S2, which also depends on a rotation parameter in the range θ ∈[−5⁰, +5⁰] with a step of variation of 0.5⁰ and for a translational parameter of −4.5 pixel along the x and y axis. (a) T2w-DTI (b-values = 500 s/mm²) registration; (b) T2w-DTI (b-values = 1250 s/mm²) registration. These curves show a certain number of local maxima. As example, (+1.5⁰; 4.1902) and (2⁰; 4.2015) for the left plot, and (+0.5⁰; 4.1995) and (2⁰; 4.2041) for the right plot*

There are some small local maxima (Fig. 5.7 c and d). They are mainly caused by a local match between pixel intensities or by the large intensity difference in intensity specific to different brain tissues in different imaging acquisition modes. Usually, these local extremes lead to misregistration. MI-based HOGs reduce the risk of falling into the local maxima and improve the robustness of the registration compared with the traditional MI measure. Sometimes these local extremes lead to erroneous records.

It can be concluded that the MI does not have good registration results for image registration when it is calculated using the information provided by the pixel intensities. When the

Eng. Toporaș (Pană) Lenuța – *Applications of DWI and DTI scanning techniques for rapid assessment of specific parameter changes in brain disease*

Chapter 5 - Original contributions on utilizing Mutual Information from DTI images for image registration

information is combined with gradient information, the registration accuracy is improved, and the difference between these parameters specific to the target and source images is minimal.

The FRE values related to the images that were subjected to the registration action by translation & rotation movements are presented in Figure 5.8. The smallest registration error FRE was 2.31 ± 1.90 pixel (or 0.6111 ± 0.5027 mm) for S1; 2.1 ± 1.65 pixel (or 0.5556 ± 0.4365 mm) for S2, and 2.48 ± 1.56 pixel (or 0.6561 ± 0.4127 mm) for S3, respectively. Comparing the MI and FRE result, the T2w-DTI registration has angles of rotation of -2^{0}, $+2^{0}$, and $+2.5^{0}$ as optimal parameters.
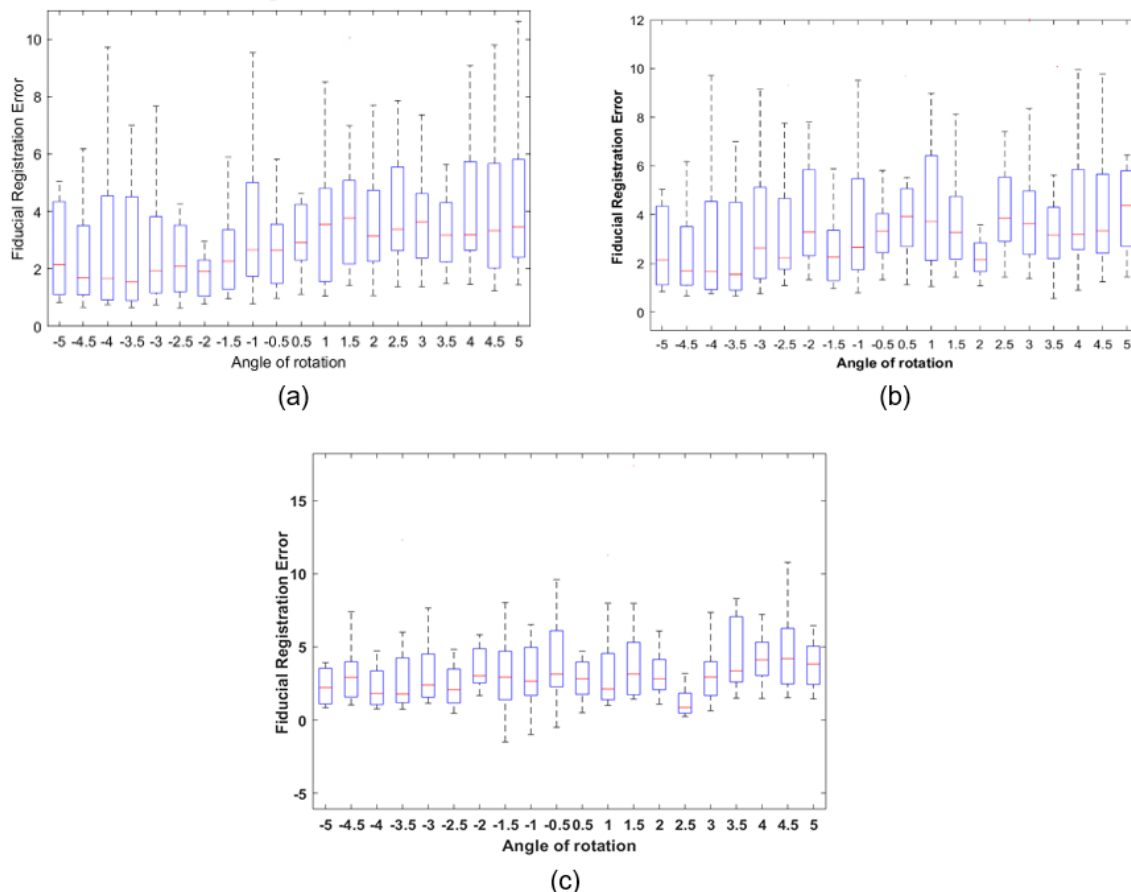

Figure 5.7 Box and whisker plot of the FRE between selected Harris corners as fiducials for T2w-DTI image registration. The registration accuracy in terms of FRE is performed for 30 control points/fiducials. (a) Subject S1; (b) subject S2; (c) subject S3.

Table 5.1 Effect of brain image multi-registration on mutual information (MI) (mean ± SD) and computation time. HOG, histogram of oriented gradients.

Registration method			MI	Computation time (s)
Healthy patient	Before registration		3.077 ± 0.163	2.33
	After translation		4.638 ± 0.421	2.48
	After global rigid registration	MI based intensities	4.018 ± 0.095	2.41
		MI based HOG	13.357 ± 0.004	2.56
Hemorrhagic patient	Before registration		3.167 ± 0.172	1.95
	After translation		4.728 ± 0.544	1.78
	After global rigid registration	MI based intensities	4.133 ± 0.132	1.95
		MI based HOG	15.355 ± 0.004	2.07
Ischemic stoke patient	Before registration		2.996 ± 0.235	1.85
	After translation		5.120 ± 0.505	1.62
	After global rigid registration	MI based intensities	4.247 ± 0.162	1.88
		MI based HOG	14.145 ± 0.004	1.97

The proposed registration method based on HOG shows good computational efficiency. The values of the computation time for each stage and registration method are shown in Table 5.1. Compared with the MI-based intensity method, the computation time for the proposed MI-based HOG increases by 6.22% for S1, 6.15% for S2, and 4.78% for S3, respectively.

The experimental results show that the registration based on the MI–HOG method improves the registration accuracy, while the computational efficiency remains almost unchanged.

The data from this study has been published in the article "*Combining Sparse and Dense Features to Improve Multi-Modal Registration for Brain DTI Images*", S. Moldovanu, **L. P. Toporaș**, A. Biswas, L. Moraru, Entropy 2020, 22, 1299, IF 2.738 [261].

Eng. Toporaș (Pană) Lenuța – *Applications of DWI and DTI scanning techniques for rapid assessment of specific parameter changes in brain disease*

Conclusions and future work

Conclusions and future work

The results presented, analyzed, and discussed in the previous chapters had relevant contributions for my research project according to the objectives proposed in the beginning of my PhD thesis.

- The textural similarity method utilized a proprietary algorithm to evaluate similarity between regions of interest in the left and right brain hemispheres. Results were evaluated using K-means clustering algorithms and Silhouette coefficient, and overall classification accuracy was assessed using ROC curves. Comparison of trend lines extracted from skeleton maps of brain images revealed that PD images preserve edges better than T2w images.
- The hit-or-miss method was employed to identify isolated pixels that were used as classifiers for identifying the existence of acute stroke. The study correlated the higher number of isolated pixels with the patients suffering stroke indicates. The proposed method is a simple, fast, and effective way to assess the presence of stroke-type pathology in MR images.
- The fractal dimension of brain in MR images was determined for healthy patients and patients with metastases. Results showed that the second-order filters such as Laplacian and LoG could satisfactorily distinguish between subjects. However, the Prewitt and Roberts filters produced edges that led to false irregularities, and the calculated fractal dimension failed to reflect the complexity of the brain image.
- Robust segmentation and 3D reconstruction of the brain tissues (white matter, gray matter, and cerebrospinal fluid) were performed on DTI images of a healthy subject that were processed using bilateral and anisotropic diffusion filters. The performance of the filters was analyzed using the first-order features, namely kurtosis and skewness. The Bland-Altman method was used as a validation technique to establish agreement between the two filtering methods. The results indicated that the anisotropic diffusion filter is a more robust and efficient pre-processing method for DTI brain images.
- The efficacy of Rician-type noise removal in DTI images was studied using Minimum and Maximum statistical filters. The filtered 2D images were also converted to 3D images. The filters' performances were evaluated using the PSNR and the Dice score value, and by comparing the volume of the 3D brain images. The results showed that the Minimum filter was more effective in removing the salt-and-pepper noise specific to these types of images. The efficiency of the median and neural network filters was also studied using brain images of patients diagnosed with multiple sclerosis and Alzheimer's. The results indicated that median filter produced the most accurate 3D reconstruction of brain tissues.
- Furthermore, the accuracy of LGC and FF segmentation methods was analyzed in the case of glioma tumor. A sound comparison using the ground truth images provided by the BraTS 2022 database was performed. The 3D tumor reconstruction and volume analysis demonstrated that the LGC algorithm provided better segmentation results, as the calculated volume is 71% of the tumor volume calculated using the ground truth images.

Eng. Toporaș (Pană) Lenuța – *Applications of DWI and DTI scanning techniques for rapid assessment of specific parameter changes in brain disease*

Conclusions and future work

− A multi-modal image registration algorithm to align T2w images, as a fixed reference, and DTI images acquired at parameters b = 500 and 1250 s/mm^2 was proposed. The algorithm was based on linear transformation and orientation of image gradients, and the Mutual Information (MI) parameter was used to calculate the statistical relationship of pixels and the histogram of oriented HOG gradients. Harris corners were employed as image-specific fiducial points to allow for image alignment. The accuracy of image registration using the HOG-oriented gradient histogram was evaluated using fiducial registration error (FRE) values, which indicated a high level of accuracy despite a 6% increase in the time required for registration.

Future research directions

− Further research could deeply explore the application of fractal analysis in studying anatomical relationships between different anatomical and/or cerebral structures.
− Other segmentation and filtering algorithms using a wider range of brain images with different acquisition conditions could also be investigated.
− Additionally, further development and improvement of 3D reconstruction of anatomical structures are an affordable aid that is useful in neurosurgery. Implementation of segmentation algorithms to facilitate modeling of an artificial 3D implant for reconstructing cranial defects and 3D printing could also be explored.
− Finally, other databases than those provided by dedicated sites could offer new insights into medical image analysis research.

Eng. Toporaș (Pană) Lenuța – *Applications of DWI and DTI scanning techniques for rapid assessment of specific parameter changes in brain disease*

Reference list

Reference list

ISI indexed journals
1. **L. Pana**, S. Moldovanu, N. Dey, A. S. Ashour, L. Moraru, "*Brain tissue evaluation based on skeleton shape and similarity analysis between hemispheres*", MDPI, Journals Computation, Volum 8, 2020, Issue 2:31, eISSN: 2079-3197, https://doi.org/10.3390/computation8020031, (IF=0, emerging), **1 cite**;
2. S. Moldovanu, **L. P. Toporaş**, A. Biswas, L. Moraru, "*Combining Sparse and Dense Features to Improve Multi-Modal Registration for Brain DTI Images*", Jour Journals Entropy, Volum 22, 2020, Issue 11, 1299, eISSN: 1099-4300, https://doi.org/10.3390/e22111299, IF=2.738, **8 cites**;

ISI Proceedings indexed volumes
1. **L. Pana**, S. Moldovanu, L. Moraru, "*Statistical Filters for Processing and Reconstruction of 3D Brain MRI*", 25th International Conference on System Theory, Control and Computing (ICSTCC), Iasi, Romania, 2021, Pages 655-658, eISSN: 2372-1618, https://10.1109/ICSTCC52150.2021.9607186;
2. **L. Pana**, S. Moldovanu, L. Moraru, "*3D Brain Tumor Volume Reconstruction and Quantification using MRI Multi-modalities Brain Images*", The 10th IEEE International Conference on E-Health and Bioengineering - EHB 2022, Grigore T. Popa University of Medicine and Pharmacy, Iași, Romania, 17-19 November 2022, Pages 1-4, eISSN: 2575-5145, https://ieeexplore.ieee.org/document/9991708/metrics#metrics;

Articles published in journal indexing in international databases
1. L. Moraru, S. Moldovanu, **L. Pana,** "*Edges Identification based on the derivative filters and fractal dimension*", Annals of "Dunarea de Jos" University of Galati, Romania, Mathematics, Physics, Theoretical Mechanics, Fascicle II, Year VIII (XXXIX) 2019, Volume 42, No. 1, Pages 34-42, https://doi.org/10.35219/ann-ugal-math-phys-mec.2019.1;
2. **L. Pana**, S. Moldovanu, L. Moraru, "*Differentiation of brain metastases in MRI image using the first- and second-order statistical features*", Annals Of "Dunarea de Jos" University of Galati, Romania, Mathematics, Physics, Theoretical Mechanics Fascicle II, Year XII (XLIII) 2020, Volume 46, No. 1, Pages 13-19, https://doi.org/10.35219/ann-ugal-math-phys-mec.2020;
3. **L. Pana**, S. Moldovanu, L. Moraru, "*3D volume reconstruction of brain tissues using nonlinear filters, k-means clustering and Bland-Altman analysis*", Annals of the University "Dunarea de Jos" of Galati, Romania, Fascicle II, Mathematics, Physics, Theoretical Mechanics, Volume 44, 2021, Issue 1, Pages 75-86, https://www.gup.ugal.ro/ugaljournals/index.php/math/article/view/4929

Articles published in the international conference volumes
1. **L. Pana**, S. Moldovanu, L. Moraru, "*Brain tissue evaluation based on skeleton shape and similarity analysis between hemispheres*", EPSMSO - 8th International Conference on Experiments/Process/System/Modeling/Simulation/ Optimization, 3-6 July, 2019, Athens, Greece, https://lfme.gr/8th-ic-epsmso-program/#1645452905480-7ab7aae2-2cc5;

Eng. Toporaș (Pană) Lenuța – *Applications of DWI and DTI scanning techniques for rapid assessment of specific parameter changes in brain disease*

Reference list

2. **L. Pana**, S. Moldovanu, L. Moraru, "*Using grey-scale hit-or-miss transform for detection of isolated foreground pixels in cerebral RMN datasets*", SGEM Conference Proceedings: 19th International Multidisciplinary Scientific GeoConference SGEM 2019, Section Advances in Biotechnology, 9 - 11 December 2019, Vienna, Austria, Volume 19, Issue 6.3, Pages 229- 236, http://10.5593/sgem2019V/6.3/S08.030;

3. S. Moldovanu, **L. Pana**, L. Moraru, "*3D volume reconstruction of brain images for common diseases of aging*", 3rd International Conference on Advances in Signal Processing and Artificial Intelligence, 17-19 November 2021, Porto, Portugal, Pages 15-17, eISBN: 978-84-09-35865-6, https://www.sensorsportal.com/ASPAI_2021/ASPAI_2021_Conference_Proceedings.pdf;

4. **L. Pana**, S. Moldovanu, L. Moraru, "*Statistical Filters for Processing and Reconstruction of 3D Brain MRI*", 25th International Conference on System Theory, Control and Computing (ICSTCC), Iasi, Romania, 2021, Pages 655-658, ISSN: 2372-1618, https://10.1109/ICSTCC52150.2021.9607186;

5. **L. Pana**, S. Moldovanu, L. Moraru, "*3D Brain Tumor Volume Reconstruction and Quantification using MRI Multi-modalities Brain Images*", The 10th IEEE International Conference on E-Health and Bioengineering - EHB 2022, Grigore T. Popa University of Medicine and Pharmacy, Iași, Romania, 17-19 November 2022, Pages 1-4, eISSN: 2575-5145, https://ieeexplore.ieee.org/document/9991708/metrics#metrics;

Participation in national and international conferences

1. L. Moraru, S. Moldovanu, **L. Pana**, "*Edges Identification based on the derivative filters and fractal dimension*", Scientific Conference of Doctoral Schools from "Dunărea de Jos" University of Galati (SCDS-UDJG 2019), 7th Edition, 13th-14th of June 2019, Galați, Romania, Section 2. Advanced Investigation Methods in Environment and BioHealth, http://www.cssd-udjg.ugal.ro/files/2019/Program_detaliat_al_conferintei_nou.pdf

2. **L. Pana**, S. Moldovanu, L. Moraru, "*Brain tissue evaluation based on skeleton shape and similarity analysis between hemispheres*", EPSMSO - 8th International Conference on Experiments/Process/System/ Modeling/ Simulation/ Optimization, 3-6 July, 2019, Athens, Greece, https://lfme.gr/8th-ic-epsmso-program/#1645452905480-7ab7aae2-2cc5

3. **L. Pana**, S. Moldovanu, L. Moraru, "*Using grey-scale hit-or-miss transform for detection of isolated foreground pixels in cerebral RMN datasets*", SGEM Conference Proceedings: 19th International Multidisciplinary Scientific GeoConference SGEM 2019, Section Advances in Biotechnology, 9 - 11 December 2019, Vienna, Austria, https://www.sgemviennagreen.org/images/deadlines/conference_programme/_Day2_Programme_POSTER.pdf

4. **L. Pana**, S. Moldovanu, L. Moraru, "*Differentiation of brain metastases in MRI image using the first- and second-order statistical features*", Scientific Conference of Doctoral Schools from "Dunărea de Jos" University of Galati SCDS-UDJG, 8th Edition, 18th -19th of June 2020, Galați, Romania, Section 2. Advanced investigation methods in environment and biohealth, http://www.cssd-udjg.ugal.ro/files/2020/program/CSSD_Section2_Program_2020_draft.pdf

5. S. Moldovanu, F.A. Damian, **L. Pana**, L. Moraru, "*Machine Learning and Artificial Intelligence for health monitoring*", International Conference Environmental

Eng. Toporaș (Pană) Lenuța – *Applications of DWI and DTI scanning techniques for rapid assessment of specific parameter changes in brain disease*

Reference list

Challenges in the Black Sea Basin: Impact on Human Health, 23 – 26 September 2020, Galati, Romania, Pages 47-47a, https://ibn.idsi.md/vizualizare_articol/115939,

6. **L. Pana**, S. Moldovanu, L. Moraru, "*3D volume reconstruction of brain tissues using nonlinear filters, k-means clustering and Bland-Altman analysis",* Scientific Conference of Doctoral Schools from "Dunărea de Jos" University of Galati SCDS-UDJG, 9th Edition, 10th- 11th of June 2021, Galați, Section 2. Advanced investigation methods in environment and biohealth,
http://www.cssd-udjg.ugal.ro/index.php/2020-2/programme-22

7. S. Moldovanu, **L. Pana**, L. Moraru, "*3D volume reconstruction of brain images for common diseases of aging"*, 3rd International Conference on Advances in Signal Processing and Artificial Intelligence, 17-19 November 2021, Porto, Portugal, https://www.sensorsportal.com/ASPAI_2021/ASPAI_2021_Conference_Programme.pdf

8. **L. Pana**, S. Moldovanu, L. Moraru, "*Statistical Filters for Processing and Reconstruction of 3D Brain MRI"*, 25th International Conference on System Theory, Control and Computing (ICSTCC), Iasi, Romania, 2021, https://icstcc2021.ac.tuiasi.ro/wp-content/uploads/2021/10/Book-of-Abstracts-ICSTCC-2021_V5-online.pdf

9. **L. Pana**, S. Moldovanu, L. Moraru, "*3D Brain Tumor Volume Reconstruction and Quantification using MRI Multi-modalities Brain Images"*, The 10th IEEE International Conference on E-Health and Bioengineering - EHB 2022, Grigore T. Popa University of Medicine and Pharmacy, Iasi, Romania, 17-19 November 2022, http://www.ehbconference.ro/Portals/18/EHB2022_Detailed_Program.pdf

10. **L. Pana**, S. Moldovanu Simona, L. Moraru, "*Similaritate în studierea imaginilor RMN 2D ale creierului uman"*, Conferința științifică: "Fizica medicală: simbioză între Fizică, Medicină și Mediu", Universitatea „Dunarea de Jos" din Galati, Romania, 28 Februarie 2019, Galaţi, Secţiunea 1: Fizică medicală; aplicații ale Fizicii în Medicină, https://www.ugal.ro/files/stiri%20si%20evenimente/program_conferinta_Fizica_medicala_2019.pdf

Eng. Toporaș (Pană) Lenuța – *Applications of DWI and DTI scanning techniques for rapid assessment of specific parameter changes in brain disease*

Selective bibliography

Selective bibliography

[1] M. Rohini, D. Surendran, *Classification of neurodegenerative disease stages using ensemble machine learning classifiers*, International Conference on recent trends in advanced computing 2019, Procedia Computer Science 165, 2019, Pages 66–73;

[2] Who european framework for action on mental health 2021-2025, https://apps.who.int/iris/bitstream/handle/10665/344609/WHO-EURO-2021-3147-42905-59865-eng.pdf?sequence=1&isAllowed=y;

[3] ***, https://www.who.int/news-room/fact-sheets/detail/the-top-10-causes-of-death;

[18] K. Iniewski, *Medical Imaging - Principles*, Detectors and Electronics, John Wiley & Sons, 2009, ISBN: 978-0-470-39164-8;

[19] R. Chandrasekaran, T.R.T. Hamizhvani, Y.K. Sowmya, B. Babu, J.E. Joseph, A. JosphineArockiaDhivya, *MRI Tumor Segmentation – An Application Approach*, International Journal of Pure and Applied Mathematics, Volume 119, 2018, Issue 18, Pages 3149-3163;

[20] M. Brazzelli, P. AG. Sandercock, F. M. Chappell, M. G. Celani, E. Righetti, N. Arestis, J. M. Wardlaw, J. J. Deeks, *Magnetic Resonance Imaging versus Computed Tomography for detection of acute vascular lesions in patients presenting with stroke symptoms*, Journal Cochrane Database of Systematic Reviews, Issue 4, 2009, PMID: 19821415;

[23] A.W. Toga și P.M. Thompson, *The role of image registration in brain mapping,* Image Vis Comput., Volume 19, 2001, Issue 1-2, Pages 3-24, http://10.1016/S0262-8856(00)00055-X;

[24] S. Pradhan, *Development of Efficient Intensity Based Registration Techniques for Multi-modal Brain Images,* PhD Thesis, Department of Electrical Engineering, National Institute of Technology, Rourkela, Odisha, India, 2016;

[28] X. Lu, S. Zhang, H. Su, Y. Chen, *Mutual information-based multimodal image registration using a novel joint histogram estimation,* Computerized Medical Imaging and Graphics, Volume 32, 2008, Issue 3, Pages 202-209;

[35] S. M. Smith, *Fast robust automated brain extraction, Human brain mapping,* Volume 17, 2002, Issue 3, Pages 143-155, http://doi:10.1002/hbm.10062;

[42] S. Moldovanu, L. Moraru, *Mass Detection and Classification in Breast Ultrasound Image using k-means Clustering Algorithm*, Proceedings of the 3rd International Symposium on Electrical and Electronics Engineering, 2010, Pages 197-201; https://doi:10.1109/ISEEE.2010.5628516;

[44] A. K. Boyat and B. K. Joshi, *Noise Models In Digital Image Processing*, Signal & Image Processing: An International Journal, Volume 6, 2015, Issue 2, Pages 63-75, http://doi.org/10.3389/fnins.2019.00909;

[49] S. U. Khana, N. Ullah, I. Ahmed, I. Ahmad, W. Y. Chai*, Comparison of MRI with other Modalities, Noise in MRI Images and Machine Learning Techniques for Noise Removal: A Review*, Curr Med Imaging rev., Volume 15, 2019, Issue 3, Pages 243-254, http://doi:10.2174/1573405614666180726124952;

[51] N. Kumar and M. Nachamai, *Noise Removal and Filtering Techniques used in Medical Images*, Oriental Journal of Computer Science & Technology, Volume 10, 2017, Pages 103–113, ISSN: 0974-6471;

Eng. Toporaș (Pană) Lenuța – *Applications of DWI and DTI scanning techniques for rapid assessment of specific parameter changes in brain disease*

Selective bibliography

[65]   Z. Rotstein, R. Hazan, Y. Barak, A. Achiron, *Perspectives in multiple sclerosis health care: special focus on the costs of multiple sclerosis*, Autoimmunity Reviews, Volum 5, Issue 8, 2006, Pages 511-516;

[69]   J. Freixenet, X. Munoz, D. Raba, J. Martı, X. Cufı, *Yet Another Survey on Image Segmentation: Region and Boundary Information Integration*, 7th European Conference on Computer (eds.) Computer Vision — ECCV, Copenhaga, Danemarca, 2002, Pages 408-422;

[71]   S. Yazdani, R. Yusof, A. Karimian, A. H. Riazi, *Brain Tissue Classification in Magnetic Resonance Images*, Jurnal Teknologi (Sciences & Engineering), Volume 72, 2015, Issue 2, Pages 29–32, ISSN 2180–3722, https://doi.org/10.11113/jt.v72.3879 ;

[78]   K. Somasundaram și T. Kalaiselvi, *A Comparative Study of Segmentation Techniques used for MR Brain Images*, Conference: Proceedings of the 2009 International Conference on Image Processing, Computer Vision, & Pattern Recognition, IPCV 2009, July 13-16, Las Vegas, Nevada, USA, Volume 9, Pages 597-603, https://doi:10.1007/s11682-018-9835-y;

[79]   J.G. Park , C. Lee, *Skull stripping based on region growing for magnetic resonance brain images*, NeuroImage, October 2009, Volume 47, Issue 4, pag.1394-1407;

[80]   H. J. Shah, *Detection of Tumor in MRI Images using Image Segmentation*, International Journal of Advance Research in Computer Science and Management Studies, Volume 2, 2014, Pages 53-56;

[87]   Mehmood, M. Muazzam, B. Muzaffar, S. Yang, A. Mehmood, M. Maqsood, M. Bashir, Y. Shuyuan, *A Deep Siamese Convolution Neural Network for Multi-Class Classification of Alzheimer Disease*, Brain Sciences, Volume 10, 2020, Issue 2, 84, https://doi.org/10.3390/brainsci10020084;

[89]   L. C. V. Harrison, M. Raunio, K. K. Holli, T. Luukkaala, S. Savio, I. Elovaara, S. Soimakallio, H. J. Eskola, P. Dastidar, *MRI Texture Analysis in Multiple Sclerosis: Toward a Clinical Analysis Protocol*, Academic Radiology, Volume 17, 2010, Issue 6, Pages 696-707, https://doi.org/10.1016/j.acra.2010.01.005;

[91]   J. Zhang, C. Yu, G. Jiang, W. Liu, L. Tong, *3D texture analysis on MRI images of Alzheimer's disease,* Brain Imaging and Behavior, Volume 6, 2012, Pages 61-69;

[95]   A. Vidyarthi and N. Mittal, *Texture based feature extraction method for classification of brain tumor MRI,* Journal of Intelligent & Fuzzy Systems, Volume 32, 2017, Issue 4, Pages 2807-2818;

[99]   A. Ishaque, R. Maani, J. Satkunam, P. Seres, D. Mah, A. H. Wilman, S. Naik, Yee-Hong Yang, S. Kalra, *Texture Analysis to Detect Cerebral Degeneration in Amyotrophic Lateral Sclerosis*, The Canadian Journal of Neurological Sciences Inc., 2018, Pages 533-539;

[101]   D. W. Shattuck, S. R. Sandor-Leahy, K. A. Schaper, D. A. Rottenberg, R. M. Leahy, Magnetic Resonance Image Tissue Classification Using a Partial Volume Model, 2001, Volum 13, Issue 5, Pages 856-876;

[109]   V. Gandhi, V. Mendiratta, S. Thakur and M. S. Choudhry, *Morphological Operations For denoising of White Gaussian Noise Corrupted MR Images*, International Conference on Electronics and Sustainable Communication Systems (ICESC), 2020, Pages 228-234, http://doi:10.1109/ICESC48915.2020.9155936;

[113]   F. J. Esteban, J. Sepulcre, J. Ruiz de Miras, J. Navas, N. Vélez de Mendizábal, J. Goñi, J. Ma Quesada, B. Bejarano, P Villoslada, *Fractal dimension analysis of grey matter in multiple sclerosis*, Journal of the Neurological Sciences, Volume 282, Issues 1–2, 2009, Pages 67-71;

Eng. Toporaș (Pană) Lenuța – *Applications of DWI and DTI scanning techniques for rapid assessment of specific parameter changes in brain disease*

Selective bibliography

[114]   S. A. Jayasuriya, A. W. C. Liewa, N. F. Law, *Brain Symmetry Plane Detection based on Fractal Analysis*, Computerized Medical Imaging and Graphics, Volume 37, Issues 7–8, 2013, Pages 568-580;

[117]   A. Di Ieva, S. Göd, G. Grabner, F. Grizzi, C. Sherif, C. Matula, *Three-dimensional susceptibility-weighted imaging at 7 T using fractal-based quantitative analysis to grade gliomas*, Neuroradiology, Volume 55, 2013, Issue 1, Pages 35–40;

[118]   J. Jiménez, A.M. López, J. Cruz, F.J. Esteban, J. Navas, P. Villoslada, J. Ruiz de Miras, *A Web platform for the interactive visualization and analysis of the 3D fractal dimension of MRI data*, Journal of Biomedical Informatics, Volume 51, 2014, Pages 176-190, https://doi.org/10.1016/j.jbi.2014.05.011;

[123]   F. T. Hoyos, R. B. Navarro, J. V. Villadiego, M. G. Martelo, *Geometrical study of Astrocytomas through Fractals and Scaling analysis, Applied Radiation and Isotopes,* Volume 141, 2018, Pages 250-256;

[124]   S. Kim, YW Park, S.H. Park, S. S. Ahn, J.H. Chang, S. H. Kim, S. K. Lee, *Comparison of Diagnostic Performance of Two-Dimensional and Three-Dimensional Fractal Dimension and Lacunarity Analyses for Predicting the Meningioma Grade*, Brain tumor research and treatment, Volume 8, 2020, Issue 1, Pages 36-42, http://doi:10.14791/btrt.2020.8.e3;

[132]   T. Kalaiselvi, P. Sriramakrishnan, R. Vasanthi, *Brain Tumor Boundary Detection from MRI Brain Scans using Edge Indication Map*‖, Proceedings of National Conferences on New Horizons in Computational Intelligence and Information Systems (NHCIIS), 2015, Pages 154-155;

[140]   W. Shen, K. Zhao, Y. Jiang, Y. Wang, Z. Zhang, X. Bai, *Object skeleton extraction in natural images by fusing scale-associated deep side outputs*, IEEE Conference on Computer Vision and Pattern Recognition, Las Vegas, NV, 2016, Pages 222-230;

[146]   H. J. Kuijf, S. J. van Veluw, M. I. Geerlings, M. A. Viergever, G. J. Biessels, K. L. Vincken, *Automatic extraction of the midsagittal surface from brain MR images using the Kullback–Leibler measure*, Neuroinformatics, Volume 12, 2014, Issue 3, Pages 395-403;

[148]   L. Moraru, M. (Visan) Punga, S. Moldovanu, *Structural Similarity Analysis for Brain MR Image Quality Assessment*, Techniques to evaluate the quality of medical images AIP Conference Proceedings 1626, Volume 39, Timisoara, Romania, 2014, Pages 137-143, https://doi.org/10.1063/1.4901358;

[149]   L. Moraru, S. Moldovanu, A. Biswas, *Edge-Based Structural Similarity Analysis in Brain MR Images*, Journal of Medical Imaging and Health Informatics, Volume 6, 2016, Issue 2, Pages 539-546;

[169]   D. Cîrneci, *Introducere în neuroștiințe*, Fundaţiei România de Mâine Publishers, 2014, ISBN:6062002088,9786062002084, https://www.academia.edu/13078609/Neurostiintele

[170]   E.T. Chou, and J.A. Carrino, *Magnetic Resonance Imaging*-Chapter 10, Pain Management WB Saunders Publishers, Philadelphia, USA Volume 1, 2007, Pages 106-117, ISSN: 0730-725X;

[171]   C. Westbrook, C. K. Roth, J. Talbot, *MRI in Practice*, Chapter 1 - Basic principles, Fourth editi on 2011, A John Wiley & Sons, Ltd., Publication, ISBN 978-1-4443-3743-3

[173]   J. Neelavalli, E.M. Haacke, I.R. Young, G.M.Bydder, Chapter 2- *Contrast Development and Manipulation in MR Imaging*, Book Magnetic Resonance Imaging of the Brain and Spine, Edited Scott W. Atlas, Philadelphia Wolters Kluwer Health/Lippincott Williams and Wilkins Publisher, Volume 1, 2009, Pages 2-24, ISBN-13:978-0-7817-6985-3;

[191]   A. Zbăganu Alexandra, I. Stănoiu, *Tehnici de detecţie de contur*, https://pdfcoffee.com/tehnici-de-detectie-conturpdf-pdf-free.html

Eng. Toporaș (Pană) Lenuța – *Applications of DWI and DTI scanning techniques for rapid assessment of specific parameter changes in brain disease*

Selective bibliography

[193] S. Moldovanu, L. Moraru, D. Bibicu, *Bio-Structural Analysis of Breast Using Fractal Analysis in Ultrasound Images*, Annals of Dunărea de Jos University Fascicle II, Anul III (XXXIV), No. 1, 2011, Pages 66-72;

[197] K. Sanjay, M. Singh, D. Shaw, *Comparative analysis of various edge detection techniques in biometric application*, International Journal of Engineering and Technology (IJET), Volume 8, 2016, Issue 6, Pages 2452-2459, ISSN (Print) :2319-8613 https://doi:10.21817/ijet/2016/v8i6/160806409;

[202] S. Kumar, M. Singh, D.K. Shaw, *Comparative Analysis of Various Edge Detection Techniques in Biometric*, International Journal of Engineering and Technology, Volume 8, 2016-2017, Issue 6, Pages 2452-2459, ISSN (Print) : 2319-8613, https://doi:10.21817/ijet/2016/v8i6/160806409;

[205] D. Yang, G. Rao, J. Martinez, A. Veeraraghavan, A. Rao, *Evaluation of tumor-derived MRI-texture features for discrimination of molecular subtypes and prediction of 12-month survival status inglioblastoma*, Med Phys., Volume 42, 2015, Issue 11, Pages 6725-6735, https://doi:10.1118/1.4934373;

[206] X. Zhang, Y. Feng, W. Chen, X. Li, A.V. Faria, Q. Feng , S. Mori, *Linear registration of brain MRI using knowledge-based multiple intermediator libraries*, Frontiers in Neuroscience, Volume 13, 2019, 13, Article 909, Pages 1-10, ISSN=1662-453X, https://doi.org/10.3389/fnins.2019.00909;

[211] P. Soille, *Morphological Image Analysis: Principles and Applications*, Second Edition, Publish by Berlin Heidelberg, Springer-Verlag, Second edition, 2003, Pages 15-32, 63-97, https://doi.org/10.1007/978-3-662-05088-0, ISBN: 978-3-662-05088-0;

[214] D. Anoraganingrum, *Cell segmentation with median filter and mathematical morphology operation,* Proceeding's 10th International Conference on Image Analysis and Processing, Venice, Italy, 27-29 September 1999, Pages 1043-1047;

[227] S. Sabaghian, H. Dehghani, S.A.H. Batouli, A. Khatibi, M. A. Oghabian, *Fully automatic 3D segmentation of the thoracolumbar spinal cord and the vertebral canal from T2-weighted MRI using K-means clustering algorithm*, Spinal Cord., Volume 58, 2020, Issue 7, Pages 811-820, https://doi.org/10.1038/s41393-020-0429-3;

[228] *Evaluarea semnelor și testelor diagnostice prin curba ROC*, https://www.info.umfcluj.ro

[230] O. Gerke, *Reporting Standards for a Bland–Altman Agreement Analysis: A Review of Methodological Reviews*, Journal Diagnostics, Volume10, 2020, Issue 5, 334, PMID: 32456091; PMCID: PMC7278016, https://doi.org/10.3390/diagnostics10050334;

[247] **L. Pana**, S. Moldovanu, N. Dey, A. S Ashour, L. Moraru, *Brain tissue evaluation based on skeleton shape and similarity analysis between hemispheres*, Journal Computation, Volume 8, 2020, Isuue 2:31, https://doi.org/10.3390/computation8020031;

[256] **L. Pana**, S. Moldovanu, L. Moraru, *Statistical Filters for Processing and Reconstruction of 3D Brain MRI*, 25th International Conference on System Theory, Control and Computing (ICSTCC), Iași, România2021, Pages 655-658, ISSN: 2372-1618, https://10.1109/ICSTCC52150.2021.9607186.

[260] **L. Pana***, S. Moldovanu, L. Moraru, *3D Brain Tumor Volume Reconstruction and Quantification using MRI Multi-modalities Brain Images,* The 10th IEEE International Conference on E-Health and Bioengineering - EHB 2022,   Grigore T. Popa University of Medicine and Pharmacy, Iasi, Romania, 2022

Eng. Toporaș (Pană) Lenuța – *Applications of DWI and DTI scanning techniques for rapid assessment of specific parameter changes in brain disease*

Selective bibliography

[261] S. Moldovanu, **L. P. Toporas**, A. Biswas, L. Moraru, *Combining Sparse and Dense Features to Improve Multi-Modal Registration for Brain DTI Images*, Entropy 2020, 22, 1299. https://doi.org/10.3390/e22111299.

Priority axis 6- Education and skills

Project title: „Programme for increasing performance and innovation in doctoral and postdoctoral research of excellence - PROINVENT"

Contract No: 62487/03.06.2022 POCU/993/6/13 - Cod SMIS: 153299